Engineered 3D liver-tissue model with minispheroids formed by a bioprinting process supported with *in situ* electrical stimulation

WonJin Kim [a], GeunHyung Kim [a,b,c,*]

[a] *Department of Precision Medicine, Sungkyunkwan University School of Medicine (SKKU-SOM), Suwon, 16419, Republic of Korea*
[b] *Institute of Quantum Biophysics, Department of Biophysics, Sungkyunkwan University, Suwon, 16419, Republic of Korea*
[c] *Biomedical Institute for Convergence at SKKU (BICS), Sungkyunkwan University, Suwon, 16419, Republic of Korea*

ARTICLE INFO

ABSTRACT

Three-dimensional (3D) bioprinting, an effective technique for building cell-laden structures providing native extracellular matrix environments, presents challenges, including inadequate cellular interactions. To address these issues, cell spheroids offer a promising solution for improving their biological functions. Particularly, minispheroids with 50–100 μm diameters exhibit enhanced cellular maturation. We propose a one-step minispheroid-forming bioprinting process incorporating electrical stimulation (E-MS-printing). By stimulating the cells, minispheroids with controlled diameters were generated by manipulating the bioink viscosity and stimulation intensity. To validate its feasibility, E-MS-printing process was applied to fabricate an engineered liver model designed to mimic the hepatic lobule unit. E-MS-printing was employed to print the hepatocyte region, followed by bioprinting the central vein using a core-shell nozzle. The resulting constructs displayed native liver-mimetic structures containing minispheroids, which facilitated improved hepatic cell maturation, functional attributes, and vessel formation. Our results demonstrate a new potential 3D liver model that can replicate native liver tissues.

1. Introduction

Three-dimensional (3D) bioprinting is an efficient fabrication technique for conveying cell-laden structures [1,2]. Bioprinting can be a good tool for effectively providing biochemical and biophysical factors to cells within printed structures [3–7]. Recently, various researchers have applied this powerful method to fabricate native extracellular matrix (ECM)-mimetic cell constructs, which have great potential for successful restoration of damaged tissues [8]. Bioprinted tissue constructs have been used not only to recover damaged bodies but also as *in vitro* models of on-chip devices to discover new drugs and personalized medical treatments [9–11].

For *in vitro* liver tissue fabrication, a bioprinting technique has been employed to build hepatic models, with a particular focus on mimicking the liver tissue-specific unit of the hexagonal-structured hepatic lobule and providing vessel formation [12,13]. Table 1 provides an overview of the previous studies on bioprinted liver models [14–21]. Particularly, X. Ma et al. [19] used a digital light processing (DLP)-based bioprinting method to fabricate a hepatic lobule-patterned liver tissue using gelatin

methacryloyl (GelMA)-based bioinks containing human induced pluripotent stem cells (hiPSCs)-derived hepatic progenitor cells (HPCs) and human umbilical vein endothelial cells (HUVECs). HPCs and HUVECs were alternately printed to obtain a vascularized hepatic lobule pattern. Kang et al. [21]. also fabricated hepatic lobules using an extrusion-based bioprinting approach attached to a preset cartilage mimicking the hexagonal pattern. They extruded hepatocyte- and endothelial cell-laden collagen bioinks into different parts of the separated cartilage to form a hepatic lobule-like structure and built a central vein lumen structure by extruding sacrificial alginate hydrogel into the center of the cartilage. These studies successfully obtained lobule-like liver models by developing bioprinting techniques, and the hepatic tissues could be applied for the restoration of damaged liver tissue as well as *in vitro* 3D liver models.

However, although advanced bioprinting processes have been proposed to build complex tissue-mimetic structures, several drawbacks, including poor cellular interactions, should still be considered when developing functional *in vitro* models [22–24]. After building a cell construct, crosslinking of the hydrogel-based bioink should be

performed to maintain the 3D shape [25]. Therefore, the cells could be embedded in the stiffened hydrogel, resulting in decreased cellular activities, efficient cell-cell interactions, and versatile exchange of oxygen and nutrients [26,27]. To address these issues, several techniques for developing functional bioinks or fabrication methods such as porous bioink [28,29], oxygen-generating factors [30,31], manipulation of partial cell densities [32], and providing external stimulation have been proposed [33,34].

Recently, the introduction of aggregated cells has enhanced cellular interactions [35,36]. In particular, cell spheroids, which are 3D culture systems that aggregate spherical cells, exhibit various biological benefits such as enhanced cell-cell interactions, secretion of abundant signaling factors (including cytokines, chemokines, and growth factors), induction of vessel formation in the surroundings, and expression of tissue-specific genes [36,37]. Hepatic cells also exhibited efficient maturation with enhanced gene expressions when cultured in cell spheroids [38,39]. From this viewpoint, combining cell spheroids with cell constructs could address the previously described limitations of the bioprinting process and provide diverse biological cues, resulting in the upregulation of cell maturation.

To obtain cell spheroid-based scaffolds, various approaches, such as mixing the prepared spheroids with hydrogels [40,41], positioning the prepared spheroids (e.g., polymer frameworks [42], Kenzan [43], and aspiration techniques [44]), and *in situ* spheroid-forming techniques [45,46], have been reported. The Kenzan method and aspiration technique have been proposed to deposit the prepared spheroids using a bioprinter, and needle arrays and hydrogel baths have been used to maintain their location and shape, respectively [43,44]. In addition, Jeon et al. [45]. developed a biodot printing method that prints cell-loaded bioink in a spherical shape within hydrogel struts to form cell aggregates without any prior preparation of spheroids. They reported that the cells self-assembled after removing soluble biomaterials, such as gelatin and hyaluronic acid, constituting the printed bioinks. These studies demonstrated the efficient formation potential of cell spheroid-based 3D constructs. However, several considerations, including complicated fabrication processes, preparation of multifaceted bioinks, application of supports that are unnecessary elements, and size of the spheroids, should be validated. Previously, we demonstrated a fabrication approach that combined cell spheroids with cell constructs using a microdroplet method and cell-loaded mineral oil [47]. In this study, mineral oil droplets were positioned within printed cell-laden bioinks, and the deposited cells exhibited self-assembly behavior after culturing and removing the oil components. While we successfully obtained hybrid structures containing cell spheroids and cell constructs,

Table 1
Previous studies for bioprinting liver structures. Description of previously reported research dealing with bioprinted liver constructs.

Method	Cells	Bioink	Strategies	Key results	Ref.
Extrusion-based bioprinting	L02	Collagen-chitosan	- Bioprinting cell-laden liver construct with a grid pattern - Addition of hepatocyte growth factor	- Improvement in liver tissue restoration and function *in vivo* - Lacks in patterning hepatic lobule - Lacks in using multiple cell types	[14]
Extrusion-based bioprinting	Huh7 HepaRG HUVEC LX-2	GelMA	- Comprising triple cells by seeding HUVECs onto the HepaRG/LX-2 mixture-laden structure - Treatment of TGF-b1 for fibrosis	- Improvement in hepatic cell function - Enabling the observation of collagen deposition - enabling the fabrication of relevant pathological model - Lacks in patterning hepatic lobule	[15]
Extrusion-based bioprinting	hiPSC-Hep	Alginate-gelatin	- Using a promising cell source for the generation of functional hepatocytes - Formation of hepatocyte spheroid by bioprinting	- Improvement in liver tissue function - Exhibiting favorable drug response - Lacks in patterning hepatic lobule - Lacks in using multiple cell types	[16]
Extrusion-based core-shell bioprinting	HepG2 HUVEC NHDF	Alginate-MC Collagen-fibrinogen-gelatin	- Using two bioinks : HUVEC/NHDF-laden collagen-based bioink : HepG2-laden alginate-based bioink - Using core (HUVEC/NHDF)-shell (HepG2) nozzle to separate cell region - Addition of human blood plasma into the shell bioink	- Formation of liver sinusoid structure - Improvement in hepatic cell maturation and its function - Improvement in vessel formation - Improvement in cellular interactions	[17]
Extrusion-based ferromagnetic bioprinting	L02 HUVEC	QCSP-chitosan-OHA	- Development of conductive bioink and ferromagnetic robot - Ferromagnetic bioprinting-based minimally invasive *in vivo* printing	- Acceptable cell viability - Enabling the *in vivo* printing - Lacks in using cells-loaded bioink for *in vivo* printing - Lacks in patterning hepatic lobule	[18]
DLP-based bioprinting	hiPSC-Hep HUVEC hASC	GelMA GelMA-GMHA	- Using two bioinks : hiPSC-Hep-laden GelMA bioink : HUVEC/hASC-laden GelMA/GMHA bioink - Using difference digital masks for patterning hepatic lobule structure	- Formation of hepatic lobule structure - Improvement in hepatic cell maturation and its function - Lacks in building thick structure	[19]
DLP-based bioprinting	hiHep	LdECM-GelMA	- Integration of LdECM to improve the printability and cell viability of GelMA bioink	- Formation of gear-like micro-pattern - Improvement in hepatic cell maturation and its function - Lacks in building hexagonal pattern - Lacks in using multiple cell types	[20]
Extrusion-based bioprinting	HepG2/C3A EA.hy 926	Collagen	- Using two bioinks : hepatic-laden collagen bioink : endothelial cell-laden collagen bioink - Using sacrificial bioink - Using hexagonally patterned preset cartilage	- Formation of hepatic lobule structure - Development of central vein structure - Improvement in hepatic cell maturation and its function - Improvement in vessel formation	[21]

L02: human hepato-carcinoma cell line; Huh7: human hepato-carcinoma cell line; HepaRG: human hepato-carcinoma cell line; HUVEC: human umbilical vein endothelial cell; LX2: human hepatic stellate cell line; GelMA: gelatin methacryloyl; TGF-b1: transforming growth factor beta 1; hiPSC-Hep: human induced pluripotent stem cell-derived hepatocyte; HepG2: human hepato-carcinoma cell line; NHDF: normal human dermal fibroblasts; MC: methylcellulose; QCSP: quaternized chitosan-g-polyaniline; CP: ; OHA: oxidized hyaluronic acid; DLP: digital light processing; hASC: human adipose-derived stem cell; GMHA: glycidal methacrylate hyaluronic acid; hiHep: human-induced hepatocyte; LdECM: liver-derived decellularized extracellular matrix; HepG2/C3A: human hepato-carcinoma cell line; EA.hy 926: immortalized human vascular endothelial cell.

some improvements were required, for instance, the complete removal of the remaining mineral oil.

In addition, manipulating spheroid size can also be essential in combining spheroids and cell constructs [48]. Large spheroids can induce apoptosis, particularly in the centrally located cells [48,49]. Furthermore, providing oxygen and nutrients to spheroids within hydrogel-based structures is challenging during culture. In contrast, some studies have reported that mini-cell aggregates with 90–100 μm diameters exhibited enhanced differentiation and maturation

capabilities into desired tissue phenotypes, including bone, cartilage, and liver [50–52]. Hence, the integration of minispheroids with cell structures should be carefully considered when building more biologically relevant tissue models.

To obtain functional tissue models by addressing these issues, we propose a one-step bioprinting process for fabricating minispheroid-laden 3D cell structures using an *in situ* electric field (E-field)-assisted bioprinting process. By subjecting human adipose-derived stem cells (hASCs) distributed in a collagen methacrylate (ColMA) bioink to
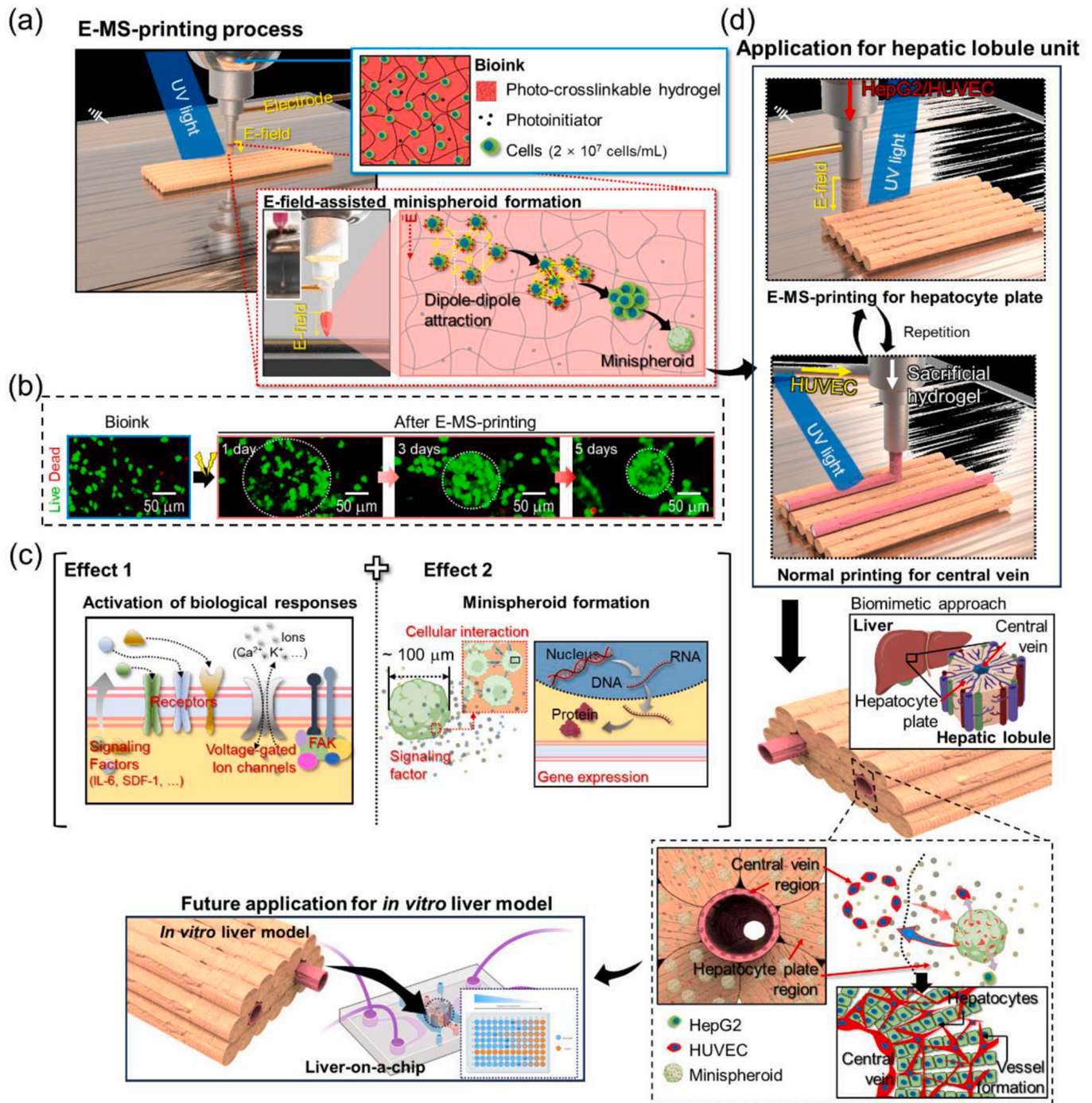
Fig. 1. Schematic illustrations for a minispheroid forming bioprinting process and an *in vitro* liver model fabrication. Schematics demonstrating (a) the *in situ* electrical stimulation-mediated minispheroid forming bioprinting (E-MS-printing) process. (b) Live (green)/dead (red) images for the bioink (before E-MS-printing) and E-MS-printed structures (1, 3, and 5 days). (c) Schematics exhibiting the expected biological responses of the E-MS-printed cells. (d) Schematics of the fabrication of hepatic lobule unit and their future application.

electrical stimulation, we observed the successful aggregation of cells and the formation of small cell aggregates. Electrical stimulation triggers various cellular responses, including alterations in membrane potential. The formation and diameter of minispheroids can be precisely controlled by manipulating fabrication parameters, such as bioink formulation and stimulation intensity. Notably, the printed minispheroids exhibited improved secretion of biological signals and factors and enhanced stem cell differentiation ability.

Moreover, our research focused on applying an *in situ* E-field-mediated minispheroid-forming bioprinting process (E-MS-printing process) to create a liver model. This model incorporates human hepatocellular carcinoma cells (HepG2) and human umbilical vein endothelial cells (HUVECs). Porcine liver-derived decellularized extracellular matrix methacrylate (LdECM-MA) was used as the base matrix for the bioink to provide an appropriate cellular microenvironment similar to that of natural liver tissue. The E-MS-printing was conducted on the HepG2/HUVEC mixture-loaded bioink to produce a hepatocyte plate region. Next, the HUVEC-loaded bioink and sacrificial hydrogel were bioprinted using a core-shell nozzle-attached normal bioprinting process to incorporate a central vein structure. The resulting constructs formed a hepatic lobule pattern containing the hepatocyte plate and central vein regions. In particular, the integration of minispheroids into liver constructs has shown promising outcomes in promoting hepatic cellular maturation, enhancing their functional attributes, and facilitating vessel formation compared to conventional constructs with uniformly distributed cells, as confirmed by immunochemical staining and gene expression analysis. Overall, our proposed fabrication strategy for producing minispheroids has the potential to build 3D models with improved biological activity and tissue function for studying tissue disorders and testing medical treatments. By creating a 3D liver model, we focused on replicating an accurate *in vivo* microenvironment and better representing the hepatic lobule structure.

2. Results and discussion

This study employed cell constructs comprising minispheroids using an *in situ* E-MS-printing process (Fig. 1a). During the E-MS-printing process, an E-field was applied to the photo-crosslinkable hydrogel-based bioink containing live cells (2.0×10^7 cells/mL), followed by crosslinking of the printed struts with UV exposure (200 mW/cm^2) under controlled printing conditions (moving speed: 5 mm/s, volume flow rate: 0.08 mL/min, and plate temperature: 37 °C). During the E-MS-printing, the E-field polarizes the cells in the bioink, inducing dipole-dipole attraction based on the dielectrophoresis (DEP) phenomenon [53,54], leading to the formation of minispheroids. The live/dead images showing the formation of minispheroids after E-MS-printing support our prediction (Fig. 1b). We predicted the electrical stimulation would have two critical effects (Fig. 1c). The applied electrical stimulation can activate diverse biological responses in each cell (effect 1), such as membrane potential, ion channel functions, focal adhesion kinase (FAK) formation, and the production of cytokines, chemokines, and growth factors [33]. In addition, stimulation could induce cellular aggregation by dipole-dipole attraction, leading to the generation of minispheroids without the spheroid preparation process before printing (effect 2). These minispheroids demonstrate improved biological functions, including cellular interactions, secretion of biological factors, and gene expression. The combined effects of electrical stimulation and minispheroid formation synergistically enhance cellular maturation and tissue functionality.

To expand the scope of the E-MS-printing process, HepG2 cells, HUVECs, and LdECM-MA were used to obtain vascularized hepatic lobule units (Fig. 1d). Electrically stimulated hepatic carcinoma cells and endothelial cells can form multicellular minispheroids that exhibit upregulated biological activities, improving cellular maturation and function. We bioprinted the sacrificial hydrogel (core region) and HUVEC-loaded bioink (shell region) to produce the central vein region

using a core-shell nozzle to build a lumen structure. This procedure was repeated to obtain a hepatic lobule-like structure. The fabricated liver tissues, consisting of the hepatocyte plate and vascular regions, can be applied to an *in vitro* 3D liver model for the organ-on-a-chip.

2.1. Setup of an E-MS-print process

Applying an electric field can induce the movement of the particles dispersed in the hydrogel. Various researchers have reported that manipulating electrical stimulation conditions can lead to the contact, rotation, alignment, and movement of particles. In our previous study, we applied an E-field in conjunction with a bioprinting process (E-printing process) to guide the alignment of stem cells loaded into a porcine muscle-derived dECM-MA (MdECM-MA) bioink [33]. In that study, *in situ* E-field stimulation and *in situ* treatment to crosslink the bioink and manipulate the electrical stimulation conditions and bioink viscosity were performed on a bioink extruded through a microscale Teflon tube, leading to the organization and formation of myofibers.

By distinguishing the E-MS-printing process from previous E-printing processes, we expect that the cells loaded in the bioink can aggregate and form minispheroids after applying an E-field by manipulating the processing conditions. In the bioink, cells can be polarized by applying an E-field, leading to the dipole-dipole attraction through stimulation (Fig. 2a). The application of the E-field to the bioink induces DEP forces, leading to the polarization of cells [54–58]. These polarized cells can move within the bioink due to the E-field. Notably, dipole-dipole contraction may occur among neighboring cells, facilitating attractive forces that bring cells together. As a result, cells aggregate within the bioink, forming minispheroids. Researchers have previously utilized this E-field-induced cell aggregation technique for trapping, tracking, and patterning cells [59–62].

The movement of particles can be estimated by a simple balance of the E-field-induced force ($F_E = \mu \cdot \nabla E$, where μ is the dipole moment and E is the applied electric field) and the viscose drag force ($F_D = 3\pi \cdot \eta \cdot d \cdot v$, where η is the viscosity of the hydrogel, d is the diameter of the particle, and v is the velocity of a particle), $F_E + F_D = 0$ [54–56]. The particles in the hydrogel are polarized by the applied E-field, exhibiting the dipole moment [$\mu = \varepsilon_o \cdot \varepsilon_c \cdot \beta_F \cdot V \cdot E$, where ε_o, ε_c, β_F, V, and E are permittivity of free space ($\varepsilon_o = 8.8542 \times 10^{-12}$ F/m), the relative dielectric constant of surrounding matrix, dimensionless parameter, volume, and E-field, respectively] [54,63]. By using the two equations, the equation related to the particle movement induced by the electric field can be simplified as follows: $dl/dt = \mu^2/(4\pi^2 \cdot l^4 \cdot \varepsilon_o \cdot \varepsilon_c \cdot \eta \cdot K^v \cdot r)$ (t is time, l is the distance between particles centers, and r is the radius of the particle). In the equation, K^v describes the particle shape, which can be approximated as $K^v \approx 1$ for the spherical particles. Based on the previous studies, the movement of spherical particles, which are arranged parallel to the E-field direction, can be simplified to estimate the required particle contact time: $t \approx 10\eta/(\varepsilon_o \cdot E^2)$. Based on the simplified equation, we can anticipate that decreasing the viscosity of the bioink or increasing the intensity of the E-field will reduce the contact time between adjacent cells, leading to the easier generation of cell aggregates. Thus, we evaluated the effects of the bioink viscosity and E-field conditions on the E-MS-printing process to select the appropriate fabrication parameters for efficient minispheroid production.

Fig. 2b–2(h) shows the effects of the bioink formulation on minispheroid formation. This section used the photo-crosslinkable collagen (ColMA) bioink containing hASCs (2.0×10^7 cells/mL) during the E-MS-printing process to establish the fabrication parameters. To evaluate the effects of ColMA concentration on the bioink, the complex viscosity (η^*) of the bioink was observed by conducting a frequency sweep using various ColMA concentrations (1.5, 2.5, and 4.5 wt%) (Fig. 2b). The results demonstrated a significant improvement in the η^* with an increasing bioink concentration (1.5 wt%: 5.0 Pa s, 2.5 wt%: 22.0 Pa s, and 4.5 wt%: 112.8 Pa s at 1 Hz frequency) (Fig. 2b).

We investigated the effects of bioink viscosity on cell contact time
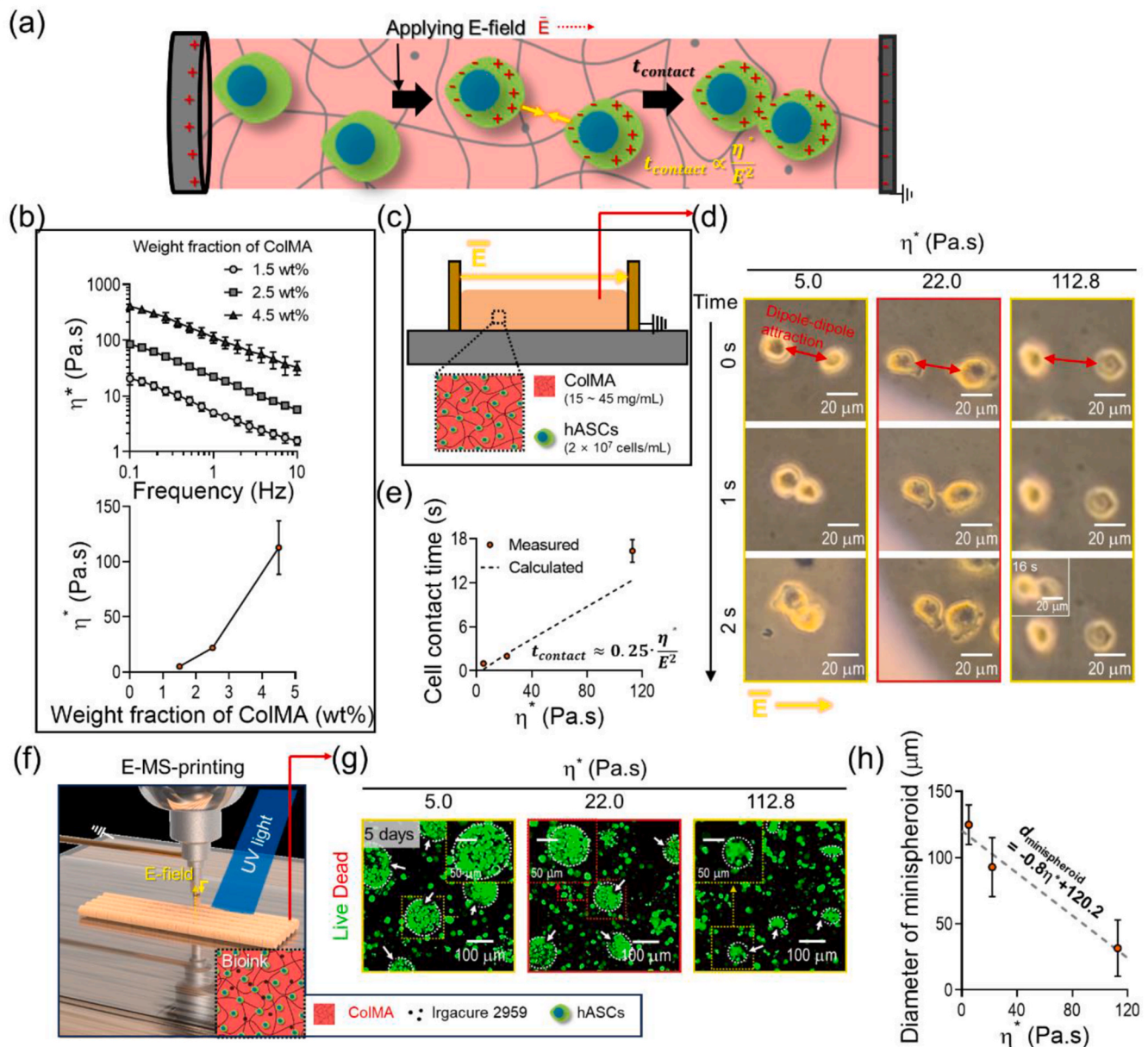
Fig. 2. Effects of the bioink viscosity on the E-MS-printing process. (a) Schematics illustrating the cellular dipole-dipole attraction phenomenon during the E-MS-printing process. (b) Complex viscosity (η^*) vs. frequency (0.1–10 Hz) and vs. collagen methacryloyl (ColMA) concentration (1.5, 2.5, and 4.5 wt%) for the bioinks (n = 3). (c) Schematic image of the designed stimulation process for observing cell contact time. (d) Optical images of the cells in the bioinks with diverse viscosity (5.0, 22.0, and 112.8 Pa s) during the E-field stimulation. (e) Required cell contact time was quantified using the images and calculated by the equation (n = 3). (f) Schematic image demonstrating the E-MS-printing process for the bioinks with various ColMA concentrations. (g) Live/dead images and (h) quantitatively evaluated the diameter of the minispheroid in the E-MS-printed three bioinks (n = 100). All data are expressed as the mean ± standard deviation (SD).

during E-field treatment by designing a simple stimulation process, as shown in Fig. 2c. The E-field was applied to ColMA bioinks with different viscosities [5.0 Pa s (video-M1), 22.0 Pa s (video-M2), and 112.8 Pa s (video-M3)] between two parallel electrodes spaced 2 mm apart. Optical images of the hASCs loaded in the bioinks were captured during E-field treatment (1.5 kV/mm) (Fig. 2d). It was observed that more time was required for two cells spaced 20 μm apart to make contact when using a bioink with a higher viscosity, as shown in Fig. 2e. These results indicate that minispheroid formation can occur more easily in a bioink with lower viscosity, as supported by the previous equation for the required particle contact time.

Supplementary video related to this article can be found at https:// doi.org/10.1016/j.bioactmat.2024.02.001

To further elucidate the formation of minispheroids, we performed

the E-MS-printing process using the hASCs (2×10^7 cells/mL)-loaded ColMA-based bioinks with diverse viscosities (5.0, 22.0, and 112.8 Pa s) under controlled fabrication conditions (moving speed: 5 mm/s, volume flow rate: 0.08 mL/min, E-field intensity: 1.5 kV/mm, plate temperature: 37 °C, and UV light: 200 mW/cm^2), as shown in Fig. 2f. After 3 days of culture, the printed cells were visualized by live (green)/dead (red) staining (Fig. 2g). As shown in the images, while aggregated cells have been observed in the three bioinks, the diameter of the minispheroids, determined using the live/dead images, gradually decreased when the viscosity of the bioink increased (Fig. 2h). Cell contact time and diameter of the obtained minispheroids followed the previously explained correlation between particle contact time and the viscosity of hydrogels during E-field treatment. We can simplify the relationship between the minispheroid diameter ($d_{\text{minispheroid}}$) and viscosity (η^*) as follows:

$d_{\text{minispheroid}} = -0.8 \cdot \eta^* + 120.2$. The findings of these investigations provide valuable insights into the relationship between bioink viscosity and minispheroid formation. While the bioink containing 1.5 wt% ColMA exhibited the probability of forming minispheroids more easily, it did not maintain its structure during the culture period (Fig. S1). Based on these results, we select 2.5 wt% ColMA ($\eta^* = 22.0$ Pa s) to fabricate minispheroid-loaded structures.

When using photo-crosslinkable hydrogel-based bioinks, UV crosslinking conditions affect the polymerization capacity of the bioinks, resulting in the maintenance of organized structures and electrically stimulated cells [33]. However, cellular activities and cell-cell adhesion can be inhibited by applying harsh crosslinking conditions, inhibiting the formation of minispheroids in the printed struts. The storage modulus (G′) has been assessed with a time sweep under various UV-light intensities (0–600 mW/cm^2, 30 s) to evaluate the effects of crosslinking conditions on the ColMA bioink. The results showed that an increase in UV light power significantly improved the G′ (Fig. S2a). In addition, we evaluated the effects of UV conditions on printability and minispheroid formation by fabrication of cell constructs under diverse UV intensities (100, 200, 400, and 600 mW/cm^2) and fixed fabrication
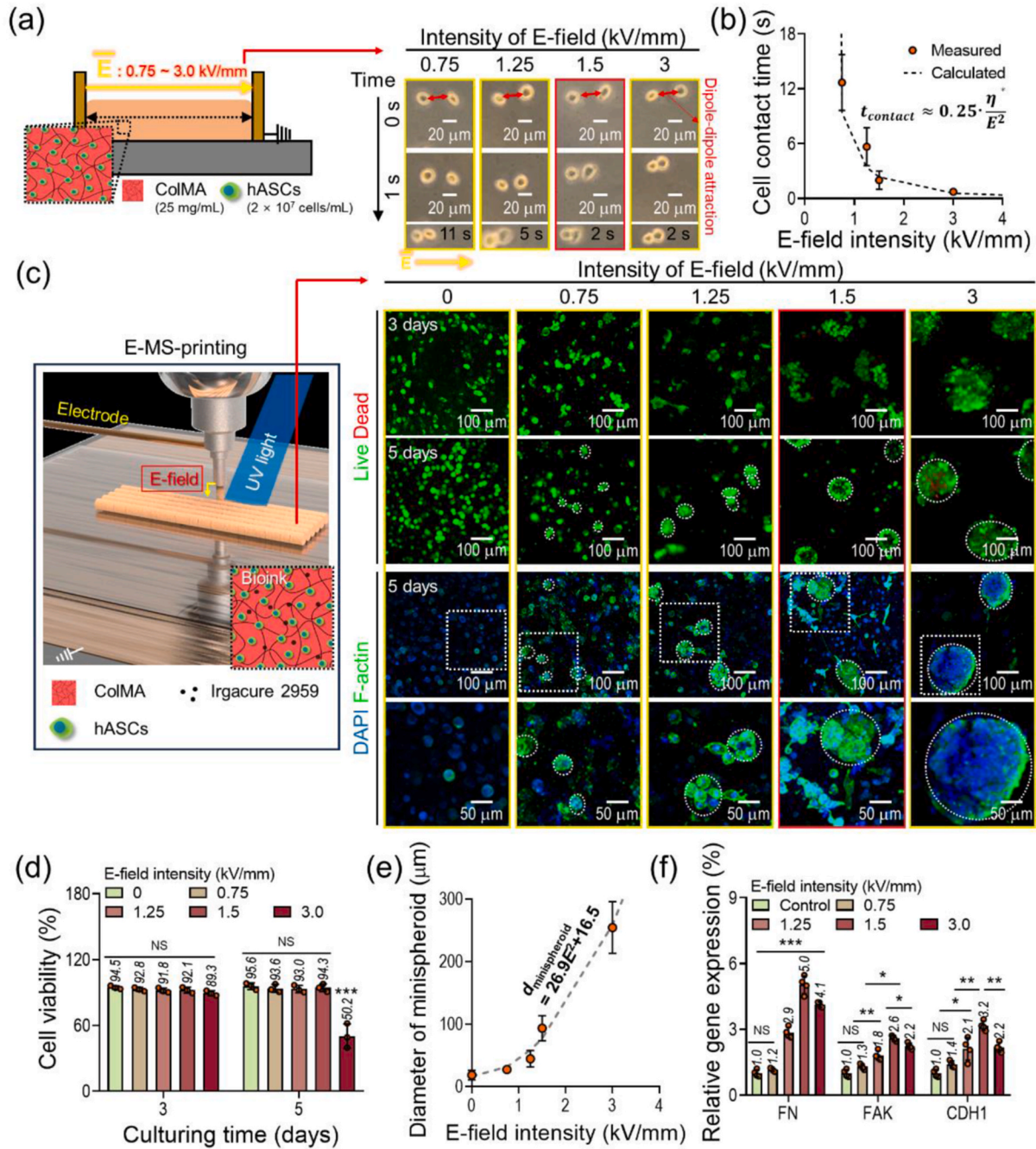
Fig. 3. Effects of the E-field conditions on the E-MS-printing process. (a) Optical images of the cells during the simplified stimulation process with diverse E-field intensities (0.75, 1.25, 1.5, and 3.0 kV/mm). (b) Required cell contact time was quantified using the optical images and calculated by the equation (n = 3). (c) Live/dead (three and five days) and DAPI (blue)/F-actin (green) (five days) of the E-MS-printed minispheroids under diverse E-field conditions. (d) Cell viability (n = 3) and (e) minispheroid diameter (n = 100) were quantitatively evaluated using the fluorescence images. (f) Expression of cellular adhesion-related genes in the E-MS-printed structures under the various E-field intensities at five days of culture (n = 4). All data are expressed as the mean ± SD. ANOVA was used to evaluate the *p*-values (*$p < 0.050$, **$p < 0.010$, and ***$p < 0.001$).

conditions (moving speed: 5 mm/s, volume flow rate: 0.08 mL/min, and E-field intensity: 1.5 kV/mm) (Fig. S2b). Printability (Pr = L^2/16A, where L and A are the perimeter and area of the pore structure, respectively [64]) and minispheroid formation were demonstrated by observing the pore structure and live/dead images, respectively. The ColMA-based bioinks exhibited acceptable printability (0.9 < Pr < 1.1) when treated with 200 mW/cm^2 or higher intensity of UV light, while the structure collapsed under 100 mW/cm^2 of UV treatment (Fig. S2c).

To further assess the effects of UV conditions, compressive properties and cellular activities of the E-MS-printed structures were observed. As expected, the compressive properties of the ColMA structures were enhanced with exposure to higher UV intensities (Fig. S2d). Conversely, the proliferation rate of hASCs in the structure decreased as the UV intensity increased, while the cell viability of all structures was above 90% (Figs. S2e and f). The results demonstrate that the increased stiffness of the bioink with enhanced UV intensity affects cell behavior. Moreover, hASC in struts treated with 400 and 600 mW/cm^2 UV power could not form minispheroids after five days of culture, but the cells successfully self-assembled after crosslinking with 100 and 200 mW/cm^2 UV light. This finding was further validated by reverse transcription polymerase chain reaction (qRT-PCR), which confirmed the decreased expression of FAK and cadherin 1 (CDH1) in the printed cell constructs crosslinked with higher UV light (Fig. S2g). These results indicate that minispheroid formation failed because of the suppressed cellular adhesion capacity. Based on these results, we selected a UV intensity of 200 mW/cm^2 for the E-MS-printing process to fabricate a structurally stable minispheroid-distributed cell construct.

When E-field stimulation was performed at various intensities, the particles exhibited different moving properties in the hydrogels. Likewise, the formation of minispheroids could be affected by the intensity of the applied E-field through the E-MS-printing process; however, cell viability could also be affected. By executing the simplified stimulation process, it was observed that less time was required for two cells spaced 20 μm apart to make contact when using higher E-field stimulation in the ColMA (2.5 wt%) bioink, as shown in Fig. 3a [video-M4 (0.75 kV/mm), video-M5 (1.27 kV/mm), video-M6 (1.5 kV/mm), and video-M7 (3.0 kV/mm)]. The required contact time was inversely proportional to the square of the electric field intensity (Fig. 3b). To observe the effects of electrical stimulation on minispheroid production, we applied diverse E-field intensities (0, 0.75, 1.25, 1.5, and 3.0 kV/mm) during the E-MS-printing process, as determined using live/dead (on days 3 and 5) and DAPI (blue)/F-actin (green) images (on day five) (Fig. 3c). The fabrication parameters (moving speed: 5 mm/s, volume flow rate: 0.08 mL/min, plate temperature: 37 °C, and nozzle-to-target distance: 2 mm) and the UV treatment (200 mW/cm^2) were fixed. We found that the printed hASCs had high cell viability (>90%) after 3 days of culture under all applied E-field conditions (Fig. 3d). However, cell apoptosis occurred in struts printed with 3.0 an E-field intensity, showing poor cell viability (50.2 ± 11.0%) after five days of culture. In contrast, high cell viability (>90%) was maintained in struts stimulated with less than 3.0 kV/mm of E-field (Fig. 3d). Regarding minispheroid formation, the diameter of the self-assembled spheroids increased as the E-field intensity increased (Fig. 3d). We can simplify the relationship between the minispheroid diameter ($d_{minispheroid}$) and E-field intensity (E) as follows: $d_{minispheroid} = 26.9 \cdot E^2 + 16.5$. In particular, the changes in the spheroid diameter based on the E-field intensity exhibited a quadratic graph shape, which corresponded to the inverse proportionality of the required contact time to the square of the E-field. Moreover, considering the E-field-induced force ($F_{E-field}$) aspect, $F_{E-field}$ is proportional to E^2 [54]. Therefore, as the generated force increases, the time required for cells to make contact decreases, and the diameter of the mini-spheroids produced during the E-MS printing improves (Fig. S3). The relationship between the minispheroid diameter and $F_{e-field}$ can be simplified as follows: $d_{minispheroid} = 0.2 \cdot F_{E-field} + 16.5$.

Supplementary video related to this article can be found at https://doi.org/10.1016/j.bioactmat.2024.02.001

To observe the cell-cell adhesion capacity of the printed minispheroids under different E-field conditions, we examined the expression of the fibronectin (FN), FAK, and CDH1 genes after five days of culture (Fig. 3f). The gene expression of hASC minispheroids gradually increased when the intensity of the E-field was increased to 1.5 kV/mm. In contrast, it was significantly reduced in the group treated with 3.0 kV/mm of E-field. The results indicated that the minispheroids produced under a 3.0 kV/mm E-field were too large (254.4 ± 41.3 μm) to receive oxygen and nutrients efficiently within the ColMA-based struts, leading to cell death. Following previous studies, we selected an E-field intensity of 1.5 kV/mm to form minispheroids with a diameter of 93.5 ± 20.1 μm, which can provide more proper cellular microenvironments than other conditions [52,65].

2.2. Comparison of E-MS-printing process with conventional spheroid forming approach

Cell spheroids exhibit an *in vivo*-mimetic microenvironment regarding reinforced cellular interactions, resulting in upregulated secretion of abundant signaling factors and tissue-specific gene expression compared to conventionally monoculture cells [35–37]. Therefore, cell spheroids can positively affect their maturation and the biological activities of the surrounding cells and tissues.

The E-MS-printed structures containing hASC minispheroids (E-MS-structure) were compared with a bioprinted ColMA structure containing hASC spheroids prepared via a microwell method (CS-structure). Conventional spheroids were prepared using an agarose mold with a cell seeding density of 1.7 × 10^4 cells/mL and cultured for 3 days to form spheroids with a diameter similar to that of the E-MS-printed minispheroids. They were mixed with ColMA hydrogel and bioprinted without electrical stimulation (Fig. 4a). Fig. 4b shows the live/dead images of the E-MS- and CS-structures after five days of culture. The images reveal comparable minispheroid diameters in both structures (E-MS-structure: 93 ± 25 μm and CS-structure: 93 ± 20 μm) (Fig. 4c and S4a). However, the minispheroids in the E-MS-structure exhibited a relatively unstable spherical shape, as indicated by the coefficient of variation (standard deviation per mean) of the spheroid diameter (E-MS-structure: 0.25 and CS-structure: 0.19) and shape analyses of sphericity and roundness [66], compared to the CS-structure (Fig. 4d).

To further evaluate the minispheroid morphologies, we observed DAPI/F-actin images of the E-MS- and CS-structures *in situ* and after 3, 5, and 10 days of culture (Fig. 4e). The images show that the gathered cells in the E-MS-structures gradually assembled to form minispheroids, and after ten days of culture, they developed cellular branches. In contrast, the conventionally prepared spheroids maintained their shape in the printed struts until ten days of culture (Fig. 4f and S4b). This phenomenon indicated that the E-MS-printed minispheroids showed relatively low cellular adhesion compared to the manually prepared spheroids, forming stretched branches after the culture periods. Conversely, the E-MS-structure exhibited a significantly higher cell proliferation rate, as evaluated by the MTT assay, than the CS-structure with tough cellular adhesion (Fig. 4g).

qRT-PCR analysis has been conducted to observe the expression of genes related to the spheroid formation (CDH1, FAK, and RhoA), signaling factor [interleukin 6 (IL6), transforming growth factor-beta 1 (TGF-b1), vascular endothelial growth factor (VEGF), and bone morphogenic protein 2 (BMP-2)], and electrical stimulation [CXCR4, stromal cell-derived factor 1 (SDF1), calcium voltage-gated channel (CACNA1C), and potassium voltage-gated channel (KCN2)]-related genes after five days of culture to validate the biological properties of the E-MS-printed minispheroids (Fig. 4h). We used bioprinted hASC-loaded ColMA bioink without an E-field (control) and conventionally prepared spheroids without formulating a bioink (spheroids) for comparative analysis. As shown in the results, genes related to the spheroid formation (CDH1, FAK, and RhoA), proinflammatory factor (IL6), and several growth factors, including TGF-b1, VEGF, and BMP-2, have been
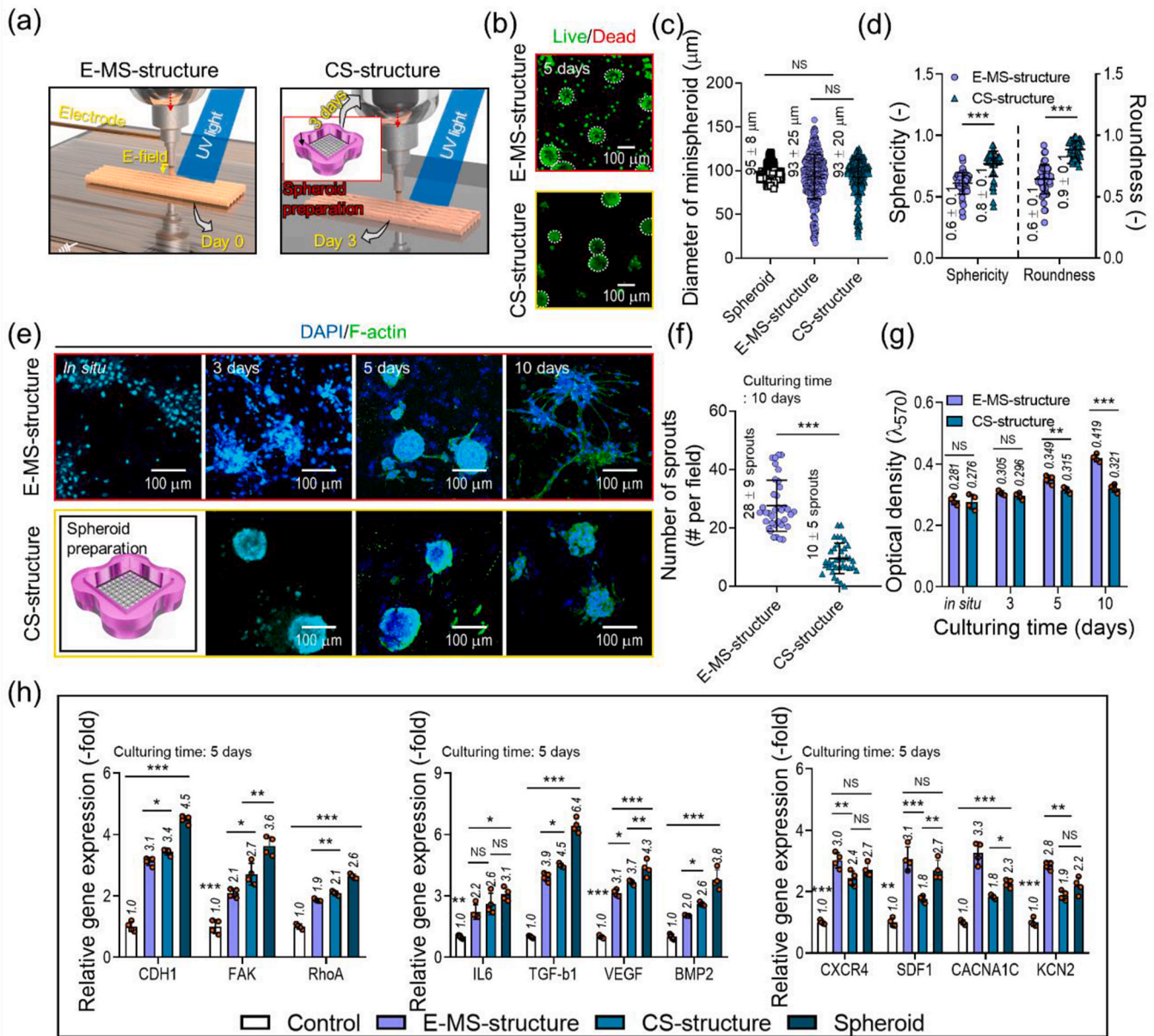
Fig. 4. Comparison of E-MS-printed minispheroids with conventionally prepared spheroids. (a) Schematics illustrating the fabrication of E-MS-printed structure (E-MS-structure) and conventionally prepared spheroid-laden structure (CS-structure). (b) Live/dead images of the E-MS- and CS-structures at five days of culture. (c) Quantitatively measured minispheroid diameter (n = 100) a high contents imaging instrument (n = 400). (d) Minispheroid shape analysis (sphericity and roundness, n = 50) using the live/dead images. (e) DAPI/F-actin images of the E-MS- and CS-structures *in situ* and 3, 5, and 10 days of culture. (f) The number of sprouts per minispheroid was measured using the high contents imaging instrument (n = 36). (g) MTT assay results of the minispheroid-bearing cell structures (n = 4). (h) Cellular adhesion, signaling factor, and electrical stimulation-related genes were expressed in the normally bioprinted control, E-MS-, and CS-structures and conventionally prepared spheroids at five days of culture (n = 4). All data are expressed as the mean $\pm$ SD. ANOVA and Student's *t*-test were used to evaluate the *p*-values (*$p < 0.050$, **$p < 0.010$, and ***$p < 0.001$).

upregulated in the bioprinted minispheroids and conventionally prepared spheroids compared to the control group, while those were relatively higher in the CS-structure compared to the E-MS-structure. In contrast, previously reported electrical stimulation-related genes, including signaling factors (CXCR4 and SDF1) and voltage-gated ion channel-related genes (CACNA1C and KCN2), were significantly activated in electrically stimulated minispheroids relative to the CS-structure as well as to the naive spheroid [33]. Gene expression results demonstrated that the developed E-MS-printing process could effectively produce minispheroid-loaded tissues without requiring complicated additional procedures. However, it exhibits reduced biological activity compared to the CS-structure. Moreover, the applied E-field stimulation activated ion channels and other signals, leading to cellular

cytoskeleton organization, proliferation, and differentiation upregulation.

In general, cell spheroids can induce the migration of surrounding cells and the formation of new vessels by secreting abundant signaling factors. Following gene expression analysis of the minispheroids, we observed their ability to induce migration and tube formation in HUVECs (Fig. 5). In this study, we collected conditioned media by incubating the control, E-MS-structure, and CS-structure (after five days of culture) in serum-free media for 3 days (Fig. 5a). A migration assay was conducted by scratching the culture plates after culturing HUVECs to create an empty region. In addition, a tube formation assay was performed by seeding HUVECs onto Matrigel-coated culture plates. The prepared conditioned media were used to observe cellular responses.
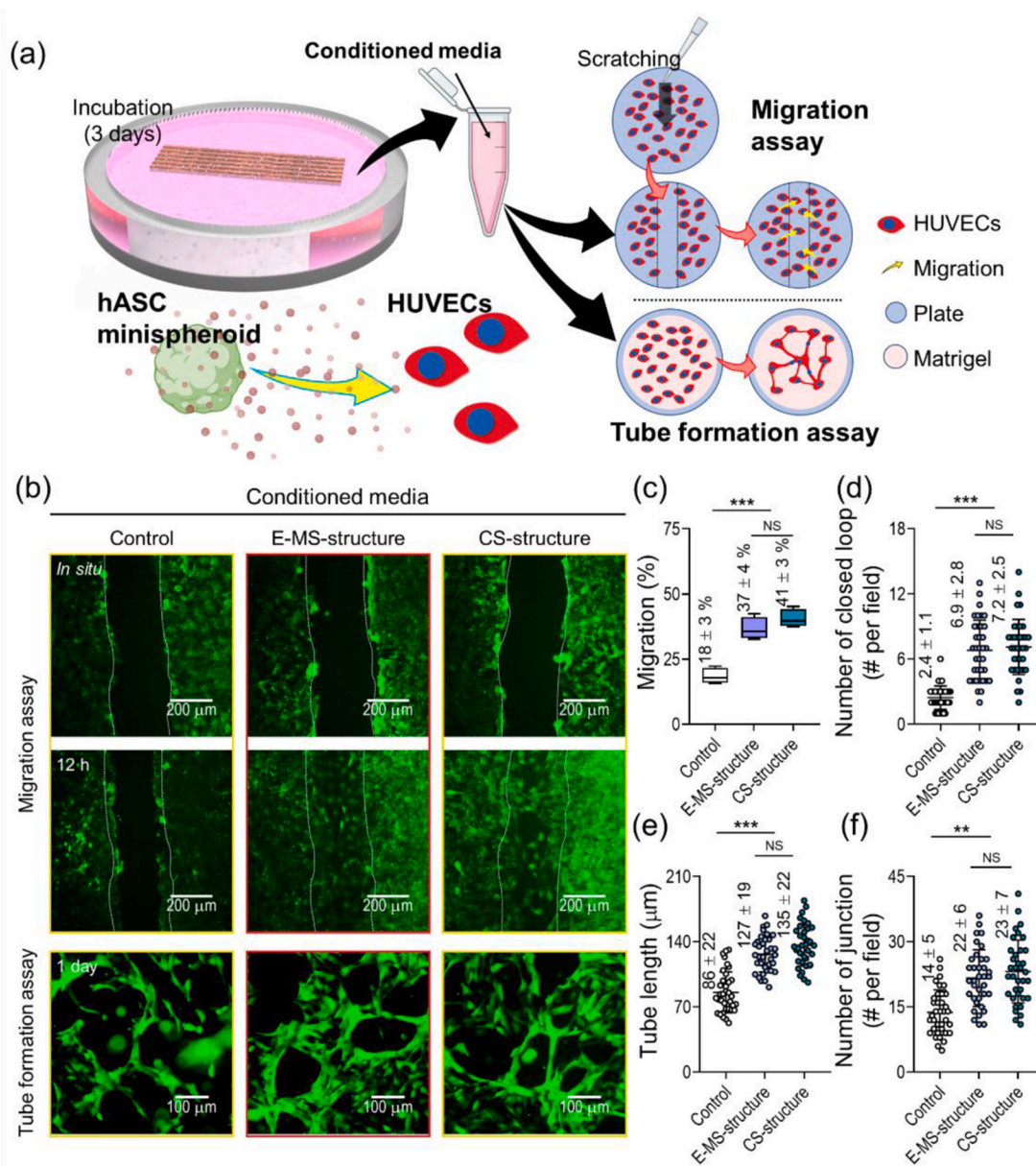
Fig. 5. Effects of minispheroids on the endothelial cell activities. (a) Illustrated schematics demonstrating the migration and tube formation assays by treating conditioned media of bioprinted structures (normally printed control and minispheroid contained E-MS- and SC-structures). (b) CellTracker (HUVEC: green) and angiogenesis analysis images captured after treating conditioned media for conducting migration (*in situ* and at 12 h) and tube formation (at day 1) assays. Quantified (c) HUVEC migration using the images (n = 4) and (d) the number of closed vascular loops, (f) tube length, and (e) the number of junctions using the high contents imaging instrument (n = 36). All data are expressed as the mean ± SD. ANOVA was used to evaluate the *p*-values (*$p < 0.050$, **$p < 0.010$, and ***$p < 0.001$).

Fig. 5b shows the green fluorescence of HUVECs in the migration (*in situ* and at 12 h) and tube formation (at day 1) assays. Both conditioned media collected from the spheroids exhibited significantly upregulated HUVEC migration (Fig. 5c), formation of closed mesh loops and vascular nodes (Fig. 5d and e), and vascular tube length (Fig. 5f) compared to the control group. In contrast, the difference between the E-MS- and CS-structures was negligible (Fig. S5).

Based on the *in vitro* biological activity assessment results, we can conclude that the E-MS-printing approach has successfully demonstrated its effectiveness in fabricating 3D cell constructs containing minispheroids, showing the efficient biological benefits of cellular interactions and maturation.

The differentiation activities of the E-MS-structure were analyzed by inducing hepatogenesis (Fig. S6). The hepatogenic medium has been treated onto the control and E-MS-structure after 7 days of culture using

the culture medium. As expected, the 3D constructs containing minispheroids exhibited significantly promoted hepatogenic differentiation compared to the control group containing only single hASCs, as validated by immunofluorescence imaging and gene expression analysis, compared to conventionally prepared spheroids. We carefully determined that this phenomenon occurred because of the improved biological responses of cells, including secretion of diverse signaling factors and activation of voltage-gated ion channels, induced by the synergistic effects of electrical field stimulation and cellular interactions in the E-MS-structure. While the induction of hASCs into hepatocyte-like cells within the E-MS-structure was observed, feasible cell sources such as hiPSCs and human hepatocytes will be employed in the E-MS-printing process in future research to apply this process for damaged liver tissue regeneration or the creation of *in vitro* liver models.

To extend the applicability of the E-MS-printing process, we applied

the E-MS structure to bone and cartilage tissues (Fig. S7). The osteogenic and chondrogenic medium has been treated onto the 3D structures after 7 days of culture using the culture medium. As expected, the hASC minispheroids exhibited significantly improved osteogenic and chondrogenic differentiation compared to the control group containing only single hASCs, as validated by immunofluorescence imaging, gene expression analysis, and calcium and glycosaminoglycans (GAGs) production. These enhancement effects are attributed to the activation of cellular responses, such as the upregulation of signaling factors like BMP-2 or TGF-b1, by the synergistic effects of E-field stimulation and cellular interactions, demonstrated in Fig. 4h [67,68].

2.3. Application of minispheroids-laden structure to hepatic tissue formation

Hepatic cells exhibited significantly enhanced cellular maturation and function when cultured in aggregated structure [38,39]. To expand the feasibility of the E-MS-printing process for hepatic tissue formation with minispheroid-loaded structures, we used LdECM-MA extracted from porcine liver tissue (Fig. S8a). LdECM-MA, where the ECM components were observed to remove almost all DNA contents (Figs. S8b and d), was used to provide a more bioactive microenvironment. Also, HepG2 human carcinoma cells, which are frequently utilized for *in vitro* hepatocarcinoma models [69,70], were employed to achieve hepatic tissue. To formulate the LdECM-MA-based bioink, we used 3 wt% LdECM-MA, which demonstrated rheological properties similar to the 2.5 wt% ColMA, applying similar fabrication conditions as the E-MS-printing process with ColMA bioink (Fig. S8e).

The effects of the E-field conditions on cell viability and minispheroid formation capacity were assessed to validate the E-MS-printing process for applying the LdECM-MA bioink (Fig. S9). Similar to the hASC-loaded ColMA bioink, HepG2 cells formed minispheroids through E-field stimulation, as shown in the live/dead images (Fig. S9a). We found that the increase in spheroid diameter with high cell viability (>90%) based on the E-field intensity from 0.75 kV/mm to 1.5 kV/mm exhibits a quadratic graph shape similar to the hASC-laden ColMA bioink (Fig. S9b). However, HepG2 cells did not effectively form minispheroids, with poor cell viability (<70%) under an E-field intensity of 3 kV/mm or higher (Fig. 5Sb). This phenomenon could be explained by previous studies reporting that crucial damage can be applied to the hepatic carcinoma cells under a certain power of electrical stimulation [71]. In particular, the E-MS-printed structures under an E-field intensity of 1.5 kV/mm exhibited the formation of minispheroid with a diameter of 92.9 ± 20.8 μm, resulting in the highest expression of spheroid formation-related genes (FN, FAK, and CDH1) at 3 days of culture and quantified albumin (ALB) + area using DAPI/ALB (green)/E-cadherin (E-cad; red) images at 14 days of culture (Figs. S9c and d). These results further validate the feasibility of using the established E-MS-printing process to produce minispheroid-integrated hepatic tissues.

A minispheroid-distributed LdECM-MA structure (MS-Ld) fabricated using the E-MS-printing process and a control structure (C-Ld) fabricated using a conventional bioprinting process without applying an E-field were used to evaluate the biological responses of the E-MS-printed HepG2 cell-laden LdECM-MA structures ($3 \times 12 \times 0.4$ mm^3) (Fig. 6a). Rheological properties of the LdECM-MA bioink were slightly increased when E-field (1.5 kV/mm) was applied [72,73], but printing behaviors including amount of extrudate bioink and printing strut size did not show significant differences (Fig. S10). Therefore, C-Ld was fabricated with processing conditions similar to the E-MS-printing. Fig. 6a shows live/dead images of both HepG2 cell-loaded structures after 1, 5, 7, and 14 days of culture, exhibiting high cell viability (>90%) (Fig. 6b). As expected, minispheroids of HepG2 cells were observed in the MS-Ld structures on day five, whereas no cell aggregates were produced in C-Ld. Fig. 6c illustrates the responses of HepG2 cells to electrical stimulation and minispheroid formation. Cells aggregated via the E-field

showed activated cell adhesion mechanisms, including fibronectin, focal adhesion kinase, and cadherins. The upregulated biological activities of HepG2 cells can accelerate several signaling pathways, such as the PI3K, MAPK, and STAT3 pathways, thereby promoting HepG2 cell maturation [74–77]. Previous studies have reported that the PI3K/AKT pathway is crucial for several cellular functions, including survival, proliferation, metabolism, and growth, and STAT3 also plays an important role in the growth and maturation of HepG2 cells [74–77]. Gene expression results validated the biological responses, exhibiting significantly enhanced expression of cell adhesion (FN, FAK, and CDH1), PI3K (PI3K and AKT), MAPK8, and STAT3-related genes in the minispheroids relative to the C-Ld structure (Fig. 6d).

In addition, to assess the hepatic cell maturation capacity of the E-MS-printed constructs, immunofluorescence, albumin and urea production, and gene expression analyses were performed (Fig. e,i). Fig. 6e shows the DAPI/ALB/E-cad ratio for the C-Ld and MS-Ld constructs after 7 and 14 days of culture. As indicated in the images, higher expression of E-cadherin and ALB was observed in the HepG2 cells of MS-Ld, exhibiting a significantly improved ALB + area compared with those of C-Ld (Fig. 6f). Likewise, albumin secretion and urea production, assessed at 1, 3, 7, and 14 days of culture, were upregulated in the minispheroids compared to HepG2 cells in the C-Ld structure throughout the culture period (Fig. 6g and h). Moreover, the expression of genes related to HepG2 cell maturation and function, including CDH1, ALB, alpha-fetoprotein (AFP), hepatocyte nuclear factor 4 alpha (HNF4A), asialo-glycoprotein receptor 1 (ASGR1), transthyretin (TTR), and cytochrome P450 1A2 (CYP1A2), was significantly upregulated in the E-MS-printed HepG2 cell constructs after 14 days (Fig. 6i). The results indicate that the activation of various signaling pathways such as PI3K/APT pathway, MAPK, and STAT3, due to the improved biological responses including secretion of signaling factors and cellular adhesion capacity resulting by the formation of minispheroids [36,37], effectively promoted HepG2 cell maturation [52,65,74–77].

2.4. Bioprinting of hepatic lobule unit with hepatic plate and central vein structures

In the human body, liver tissue consists of an anatomically unique structure, the hepatic lobule, comprising densely linked hepatocytes and vessels. To effectively regenerate damaged liver tissues or achieve *in vitro* liver models, the anatomical structure and physiological functions of the native tissue should be considered. In recent, various researchers have reported on diverse strategies to achieve 3D *in vitro* liver models, including vascular/biliary system [78], organoid [79], and spheroids-loaded hydrogel liver buds [80]. Moreover, some studies have proposed fabricating 3D hepatic tissues with hepatic lobule patterns using diverse fabrication approaches to emulate the liver tissue microenvironment further.

We aimed to fabricate a hepatic lobule unit containing a hepatocyte plate and central vein regions by employing two types of bioinks, namely LV-bioink (HepG2/HUVEC mixture-laden 3 wt% LdECM-MA bioink) and V-bioink (HUVEC-laden 3 wt% LdECM-MA bioink), along with a sacrificial hyaluronic acid (40 mg/mL) hydrogel (Hydrogel-HA) (Table 2). For the hepatocyte plate region, the LV-bioink was printed via the E-MS-printing process, followed by the fabrication of the central vein through the bioprinting process connected to a core (Hydrogel-HA)-shell (V-bioink) nozzle (Fig. 7a). The volume flow rate of the Hydrogel-HA (core region, 0.03 mL/min) and V-bioink (shell region, 0.02 mL/min) was fixed to form a central vein structure with 135.3 ± 8.1 μm inner diameter and 27.1 ± 3.1 μm wall thickness following the native tissue (Fig. S11). The fabrication steps were alternately repeated to obtain the 3D structure (experimental structure) with the proper location of the hepatocyte plate and central vein regions of the hepatic lobule, and the removal of the sacrificial hydrogel-HA during the culture period led to the formation of a hollow-shaped central vein. This bioprinted hepatic lobule unit can maintain its structure stably in the culture medium
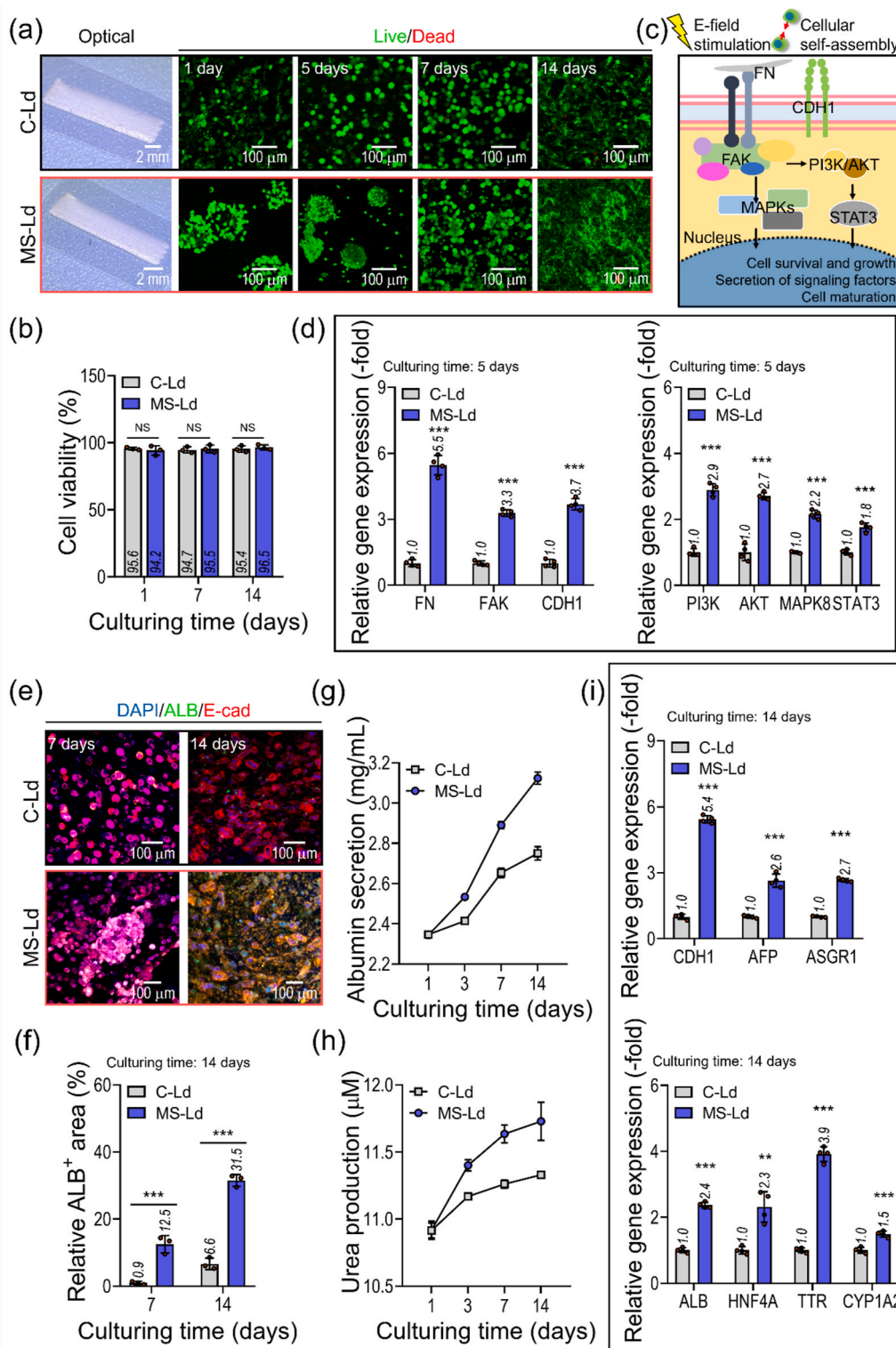
Fig. 6. *In vitro* **cellular activities of the E-MS-printed HepG2 cells.** (a) Optical and live/dead images (at 1, 5, 7, and 14 days) and (b) calculated cell viability (1, 7, and 14 days) of E-MS-printed HepG2 minispheroids-loaded liver decellularized extracellular matrix methacrylate (LdECM-MA) structure (MS-Ld structure; $3 \times 12 \times 0.4$ mm^3) and conventionally bioprinted LdECM-MA structure (C-Ld structure; $3 \times 12 \times 0.4$ mm^3) (n = 3). (c) Schematic image of the predicted biological responses of the E-MS-printed HepG2 cells. (d) Expression levels of cellular adhesion- and signaling pathways-related genes in the MS-Ld and C-Ld constructs at five days of culture (n = 4). (e) DAPI/ALB (green)/E-cadherin (E-cad, red) images and (f) quantified ALB + area for the two cell constructs at 7 and 14 days of culture (n = 3). (g) Albumin secretion and (h) Urea production results (n = 3). (i) Expression of HepG2 cell maturation- and function-related genes in the C-Ld and MS-Ld at 14 days of culture (n = 4). All data are expressed as the mean ± SD. Student's *t*-test was used to evaluate the *p*-values (**$p < 0.010$ and ***$p < 0.001$).

Table 2

Composition of bioinks. Information of bioink formulations applied for *in vitro* liver model.

	LdECM-MA (mg/mL)	HA (mg/mL)	Irgacure 2959 (mg/mL)	HepG2 (cells/mL)	HUVEC (cells/mL)
LV-bioink	30	–	3	1.2×10^7	0.8×10^7
V-bioink	30	–	3	–	2.0×10^7
Hydrogel-HA	–	40	–	–	–

LdECM-MA: porcine liver-derived decellularized extracellular matrix methacrylate, HA: hyaluronic acid, HUVEC: human umbilical vein endothelial cell.

during the culture periods, making it suitable for use as an *in vitro* model, while the 3D structure was fully collapsed in the collagenase solution (0.1 U/mL) at 21 days (Fig. S12). In the fabrication of the hepatic lobule unit, the combination of the E-MS-printed HepG2/HUVEC hybrid minispheroids and HUVEC-loaded central vein facilitated synergistic crosstalk by improving signaling factor production of the minispheroids.

Before formulating the LV-bioink, we assessed the cellular responses based on various mixture ratios of HepG2 and HUVEC (1.8:0.2, 1.6:0.4, 1.2:0.8, and 1.0:1.0) (Fig. S13). Immunofluorescence imaging and gene expression analyses demonstrated that increased HUVEC content resulted in the downregulation of the ALB + area and expression of HepG2-related genes (ALB and CDH1). In contrast, the CD31$^+$ area and expression of HUVEC-related genes (PECAM1 and CDH5) were enhanced (Figs. S13b and c). In the case of tube formation, the initial HUVEC containment affected tube formation, as assessed by culturing HepG2/HUVEC mixtures on Matrigel-coated culture plates using culture media (Fig. S13d). When HUVEC density increased, improved tube formation, confirmed by the evaluation of closed vascular loops and junctions and total tube length, was observed (Figs. S13e and g). However, the difference in HUVEC activity between the mixture ratio of 1.2:0.8 and 1.0:1.0 was insignificant. As reported previously, this phenomenon was also attributed to the mixed HepG2 cells supporting HUVEC activity [81]. Based on these results, we formulated an LV bioink by mixing HepG2 cells and HUVCEs at a ratio of 1.2:0.8.

To assess the cellular activities of the bioprinted hepatic lobule unit ($3 \times 8 \times 12$ mm^3), we printed a control group using the same fabrication methods as the experimental group but without applying E-field stimulation (Fig. 7b). Fig. 7b shows DAPI/ALB/CD31 (red) images of the hepatic lobule units after 21 days of culture. Stained images were captured using a vertical cross-sectional plane. The images revealed central vein structures with lumens and hepatocyte plate regions containing HepG2 cells and capillary networks in both the control and experimental structures. However, hybrid minispheroids in the experimental group affected their maturation and central vein formation, resulting in significantly increased ALB+ and CD31$^+$ areas compared to the control group (Fig. 7c).

Moreover, improved albumin secretion and urea production were observed in the experimental group compared to the control group during the culture period (at 1, 3, 7, 14, and 21 days) (Fig. 7d and e). Likewise, the expression of HepG2 cell- and HUVEC-related genes was upregulated in the experimental group after 21 days of culture (Fig. 7f). Based on these results, we concluded that synergistically reinforced cellular crosstalk occurred through the fabrication of electrically stimulated minispheroids, leading to the effective formation of the hepatic lobule unit.

To confirm the applicability of bioprinted hepatic lobule unit (Experimental group) as an *in vitro* liver model, a simple *in vitro* chip was prepared using agarose mold to perform perfusion cultivation (Fig. 8). The 3D liver structure was located on the simple chip and cultured under medium perfusion (20 μL/min [82,83]) environment (perfusion group) after 7 days of static culture (Fig. 8a). At 21 days, significantly promoted vessel formation and HepG2 cell activities were observed in the perfusion group with well-organized vessels, as assessed by

immunofluorescence image, albumin secretion, and urea production, compared to those in the static cultured liver structures (Fig. 8b–e). Additionally, HepG2 cell- and HUVEC-related gene expression analysis, conducted using qRT-PCR, further supported these findings (Fig. 8f). These results can be attributed to the enhancement of vessel formation and hepatic cell activities through shear stress and nutrient delivery induced by perfusion system [82–84]. With further improvements to the *in vitro* perfusion chip platform, the HepG2/HUVEC-loaded hepatic lobule unit could be utilized as an *in vitro* model, including a hepatocarcinoma model [69,70].

Although we successfully fabricated a hepatic lobule unit using a combination of the E-MS-printing and core-shell nozzle-attached bioprinting processes, further advancement of the on-a-chip platform and the application of feasible cell sources, such as human hepatocytes and hiPSCs, should be considered when applying the hybrid structure as a large-scale *in vitro* model to imitate the physiological properties of native tissues better. In addition, a more detailed design of the liver model, such as introducing the bile duct and portal vessels, should be considered in future studies to display the anatomical and physiological properties of the native liver more appropriately.

3. Conclusion

This study proposes an E-MS-printing process designed to fabricate cell constructs integrated with minispheroids that show robust biological activities. Using hASC-bearing ColMA bioink, we established an *in situ* electrical stimulation-combined bioprinting process to generate minispheroids. Our selection of parameters, including bioink viscosity and E-field conditions, produced minispheroids with diameters ranging from 90 to 100 μm. These constructs exhibited notable upregulation of biological activities, such as cellular adhesion-related gene expression, secretion of signaling factors, and facilitation of migration and tube formation of surrounding endothelial cells, compared to the cell constructs bioprinted without an E-field. Although further improvements are needed to accomplish those biological benefits compared to the conventionally prepared spheroids, the E-MS-printed minispheroids demonstrated the activation of membrane proteins, ion channels, and differentiation capacities of the stimulated stem cells.

Additionally, our approach effectively overcomes the complexities of fabricating cell constructs using conventionally prepared spheroids. HepG2 cells, HUVECs, and LdECM-MA were used to fabricate hepatic tissue to confirm the feasibility of our E-MS-printing process. The E-MS-printed HepG2 minispheroids exhibited significantly improved cellular maturation and function as assessed by immunofluorescence imaging, albumin and urea production, and gene expression analysis. Furthermore, we successfully produced a hepatic lobule structure by combining the E-MS-printed HepG2/HUVEC mixture-loaded LdECM-MA structure (hepatocyte plate region) and the core-shell nozzle-mediated HUVEC-loaded LdECM-MA hollow structure (central vein region). This approach promoted HUVEC and HepG2 cell maturation compared with the hepatic unit fabricated without electrical stimulation. Based on our findings, E-field stimulation-assisted bioprinting has the potential to produce tissue models containing minispheroids with abundant biological benefits, thereby offering new possibilities for the production of functional and physiologically relevant tissue constructs. In addition, the proposed hepatic lobule unit built using our fabrication approach can be applied as an *in vitro* liver model in future studies with further improvements.

4. Experimental section

4.1. Cell culture

The present study used hASCs (Lonza, Basel, Switzerland) to establish an E-MS-printing process. Dulbecco's modified Eagle's medium low glucose (DMEM-L; Sigma-Aldrich, USA) containing 10% fetal bovine
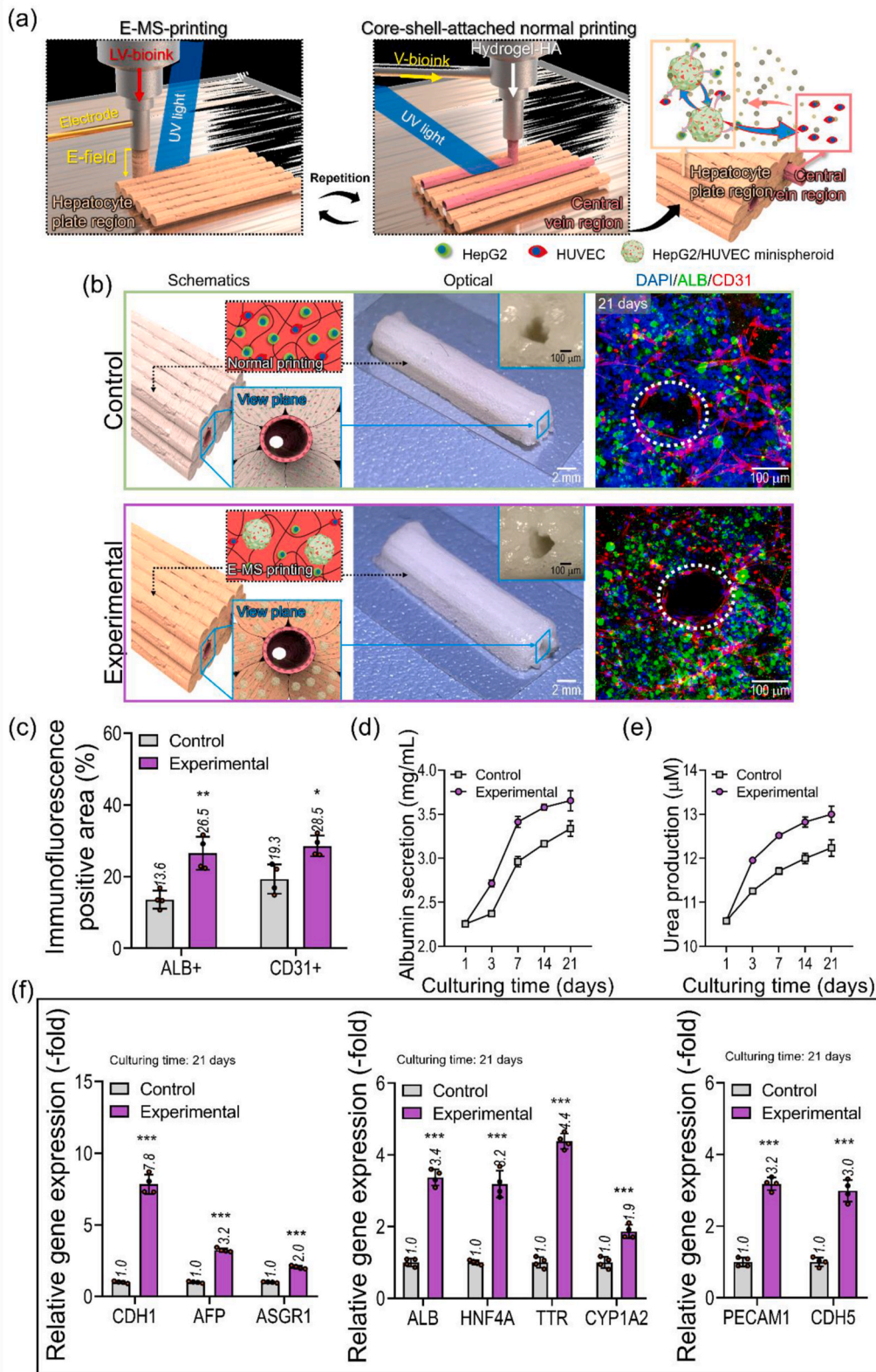
Fig. 7. Fabrication of *in vitro* liver model. (a) Illustrated schematics of the fabrication of hepatic lobule unit using the combination of E-MS-printing and core-shell-nozzle-attached normal bioprinting procedures. (b) Schematic, optical, and DAPI/ALB/CD31 (red) (at 21 days) images of the bioprinted liver models ($3 \times 8 \times 12$ mm^3) with (Experimental) and without (Control) E-field stimulation. (d) Quantification of ALB+ and CD31$^+$ areas of the Control and Experimental groups at 21 days (n = 4). (e) Albumin secretion and (f) urea production of the liver units during the culture periods (1, 3, 7, 14, and 21 days) (n = 3). (g) HepG2 cell- and endothelial cell-related genes were expressed in the control and experimental structures at 21 days of culture (n = 4). All data are expressed as the mean $\pm$ SD. Student's *t*-test was used to evaluate the *p*-values (***$p < 0.001$).
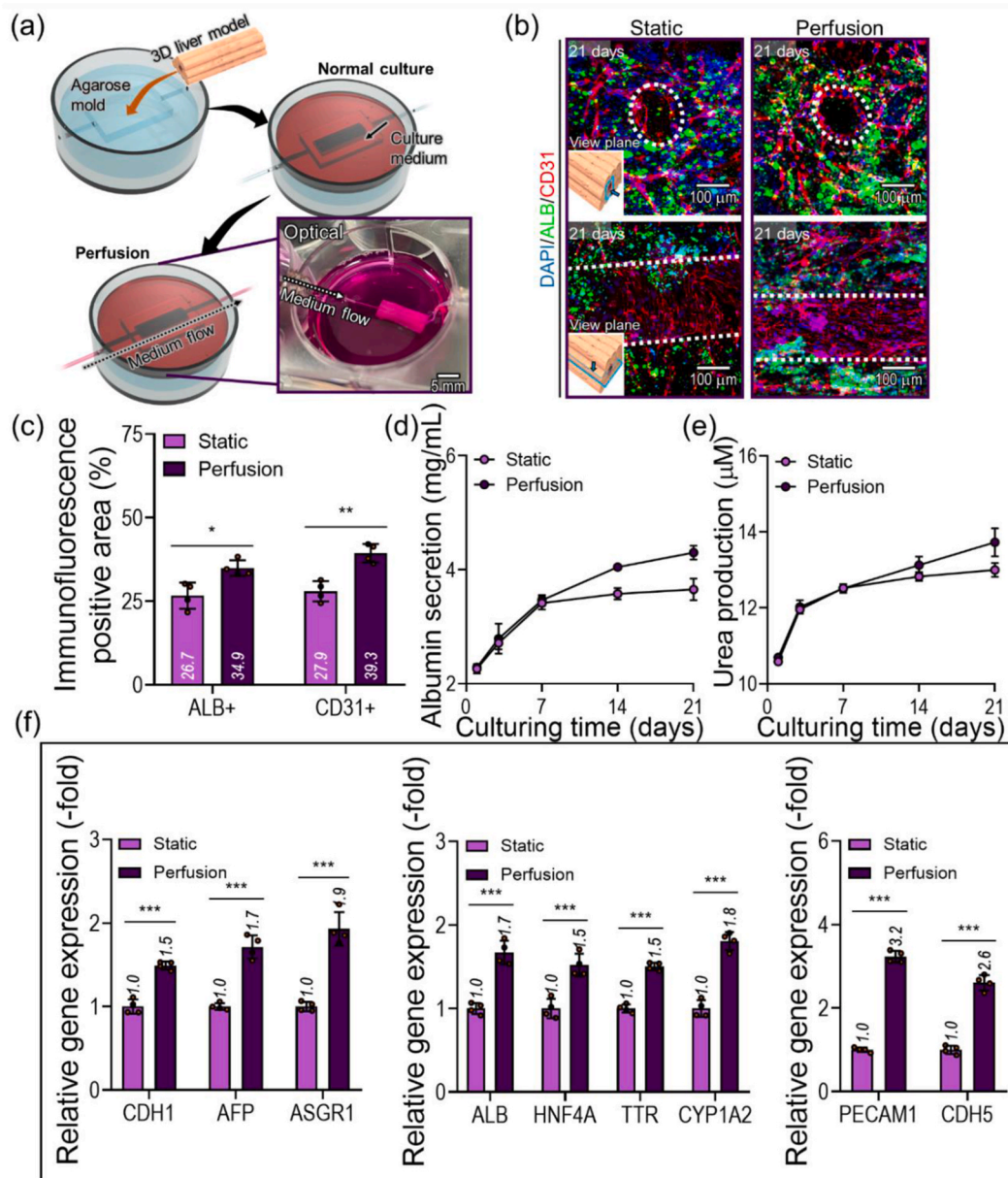
Fig. 8. *In vitro* **cellular response of bioprinted 3D liver model cultured under medium perfusion environment.** (a) Schematic and optical images demonstrating the preparation of the perfusion culture platform. (b) DAPI/ALB/CD31 stained transverse and longitudinal cross-section images of the *in vitro* liver model cultured under static (Static group) and perfusion environment (Perfusion group) at 21 days. (c) Quantitatively estimated ALB+ and CD31$^+$ areas for the *in vitro* liver model cultured with and without (Static group) medium perfusion at 21 days ($n = 4$). (d) Albumin secretion and (e) urea production of the Static and Perfusion groups (1, 3, 7, 14, and 21 days) ($n = 3$). (f) HepG2 cell- and endothelial cell-related genes were expressed in the 3D liver model cultured under static and perfusion environments at 21 days of culture ($n = 4$). All data are expressed as the mean ± SD. Student's *t*-test was used to evaluate the *p*-values (*$p < 0.05$, **$p < 0.01$, and ***$p < 0.001$).

serum (FBS; Biowest, France) and 1% penicillin/streptomycin (PS; Gibco, USA) was used to culture the hASCs. HepG2 cells (Korean Cell Line Bank, South Korea) and HUVECs (Lonza, USA) were fabricating minispheroid-loaded liver tissues. Minimum essential medium (MEM) (Gibco, USA) containing 10% FBS, 1% PS, 25 mM HEPES (Sigma-Aldrich, USA), 25 mM Sodium Bicarbonate (Sigma-Aldrich, USA), and EBM™-2 Bullet Kit™ (EBM; Lonza, USA) containing 10% FBS and 1% PS were used to culture HepG2 cells and HUVECs, respectively. The cells were incubated at 37 °C with 5% CO_2, and the culture medium was changed every two days.

4.2. Preparation of photo-crosslinkable bioinks

To formulate the photo-crosslinkable collagen bioink, collagen methacrylate (ColMA) was prepared according to a previously reported protocol [85]. Briefly, the collagen sponge was dissolved in 0.5 M acetic acid (AA; Sigma-Aldrich, USA) solution (3.75 mg/mL; adjusted to pH 8–9 by the addition of 1 M NaOH), followed by the addition of methacrylic anhydride (621 mg per 600 mg of collagen) at 4 °C for 3 days under continuous stirring. The solution was placed in a dialysis tube (1000 kDa molecular cut-off; Spectrum Chemical Manufacturing, USA) at 4 °C for 3 days. The dialyzed ColMA solution was lyophilized and stored at 80 °C before use. In particular, the ratio of methacrylation was ~79.3%, as evaluated using a 2,4,6-trinitrobenzene sulfonic acid (TNBS)

assay kit (Thermo Fisher Scientific, USA) according to a previously reported protocol [68].

Liver dECM methacrylate (LdECM-MA) was prepared as previously reported [86,87]. Briefly, liver tissues obtained from Yorkshire pigs (female; 10–15 months old) were cut into cubes ($<8 \times 8 \times 3$ mm^3) after removing the remaining blood. The minced cubes were decellularized using a 1% w/v sodium dodecyl sulfate solution until they became transparent, followed by treatment with 1% Triton X-100 (two days), 1% PS (1 h), and DNase I solution (2 h). Between treatments, tissues were rinsed thrice with Dulbecco's phosphate-buffered saline (DPBS; Biowest) and deionized water (DW). A freeze dryer (SFDSM06; Samwon, South Korea) was used to lyophilize the treated tissues. Then, the dried tissues (1 mg LdECM per 100 μL solution) were solubilized by treating 0.1 w/v% pepsin solution in 0.5 M AA at room temperature. The digested tissues were precipitated by the addition of sodium chloride powder, followed by dialysis of the precipitated matrix using a dialysis tube (1000 kDa molecular cut-off; Spectrum Chemical Manufacturing, USA) at 4 °C for 3 days. The dialyzed LdECM solution was freeze-dried and stored at −80 °C before use.

The methacrylation process was performed on the LdECM dissolved in 0.5 M AA solution (3.75 mg/mL; adjusted to pH 8–9 by adding 1 M NaOH) to obtain photo-crosslinkable LdECM.[33] Methacrylic anhydride (621 mg per 600 mg of LdECM) was added to the solution at 4 °C for 3 days under continuous stirring. The chemically modified solution was dialyzed, lyophilized, and stored at −80 °C before use. All chemical reagents used to obtain LdECM-MA were purchased from Sigma-Aldrich (USA). The ratio of methacrylation was approximately 78.2%, as evaluated using a TNBS assay kit.

PicoGreen (for DNA; Thermo Fisher Scientific), soluble collagen (Biocolor Live Sciences Assays, UK), Blyscan sulfate glycosaminoglycan (Biocolor Live Sciences Assays, UK), and Fastin elastin (Biocolor Live Sciences Assays, UK) assay kits were used to assess the remaining DNA and ECM contents. Analyses were conducted according to the manufacturer's protocols as previously described [86].

The prepared ColMA and LdECM-MA sponges were dissolved in 0.1 M AA and mixed with 10 × DMEM solution at a 1:1 ratio to neutralize the solutions to formulate the photo-crosslinkable bioinks. Then, the hydrogels were mixed with cells (cell density: 2.0×10^7 cells/mL) and 3 w/v% photoinitiator, 2-hydroxy-4'-(2-hydroxyethoxy)-2-methyl-propiophenone (Irgacure 2959; Sigma-Aldrich, USA). ColMA bioink was prepared by mixing hASCs (2.0×10^7 cells/mL) with ColMA hydrogel. HepG2 cells were mixed with the LdECM-MA bioink to perform the E-MS-printing to observe the formation of hepatocyte minispheroids. For the LV-bioink, a mixture of HepG2 cells and HUVECs was added to the LdECM-MA hydrogel, whereas HUVECs were mixed with the LdECM-MA hydrogel to formulate the V-bioink. The final densities of ColMA and LdECM-MA were 25 mg/mL and 30 mg/mL, respectively.

4.3. Fabrication of minispheroids-loaded structures and vascularized hepatic lobules

hASC-laden ColMA, HepG2-laden LdECM-MA, and LV bioinks were bioprinted using the E-MS-printing process consisting of a 3D bioprinting system (DTR3-2210 T-SG; DASA Robot, South Korea) supplemented with a pneumatic dispenser (AD-3000C, Ugin-tech, South Korea) and a high-voltage direct-current (HVDC) power supply (SHV300RD-50K; ConverTech, South Korea) to apply the E-field during the bioprinting process. A copper-clad aluminum wire attached the HVDC power supply to the nozzle tip. The bioinks were printed onto a copper-based grounded electrode target covered by a sterilized PET film through a 30G microscale nozzle, and voltage was simultaneously applied to the E-field. The printing speed (5 mm/s), volume flow rate (0.08 mL/min), and temperature conditions (target: 37 °C and barrel/nozzle: 25 °C) were controlled. The extruded bioinks were crosslinked by exposure to UV light (200 mW/cm^2). As a control, bioinks were printed under the same fabrication conditions without an E-field.

LV-bioink, V-bioink, and hyaluronic acid hydrogel (hydrogel-HA) (40 mg/mL in DPBS; Sigma-Aldrich, South Korea) were used to obtain vascularized hepatic lobules. The E-MS-printing process was used to print the LV bioink for the hepatocyte plate structure. In the case of the central vein structure, hydrogel-HA and V-bioinks were printed using a normal bioprinting process (without E-field) connected with a core (hydrogel-HA)-shell (V-bioink) nozzle with controlled volume flow rates (core: 0.03 mL/min and shell: 0.02 mL/min). The printing speed (5 mm/s) and temperature conditions (target: 37 °C and barrel/nozzle: 25 °C) have been controlled, and the extruded bioinks were crosslinked by UV light (200 mW/cm^2). To obtain the hepatic lobule structure, the E-MS-printing and core-shell-attached normal printing procedures were alternately repeated by positioning both the hepatocyte plate and central vein properly. As a control, a normal bioprinting process was used to fabricate the hepatocyte plate region without the E-MS-printing process.

4.4. Preparation of conventional spheroids-laden structure

According to the manufacturer's protocols, agarose molds were used to prepare the conventional hASC-minispheroids (~100 μm diameter) to verify the efficacy of generated E-MS-printed minispheroids. Briefly, a 2% agarose hydrogel (in DPBS; Invitrogen, USA) was cast into a 3D Petri dish (Sigma-Aldrich, USA) to fabricate agarose molds. Then, the hASCs (190 μl; 1.7×10^4 cells/ml) were seeded into the prepared molds and cultured for 3 days with the DMEM-L.

To fabricate the conventionally prepared spheroid-laden structures (CS-structure), we printed ColMA (2.5% wt) bioink mixed with a photoinitiator (3% w/v). We prepared hASC spheroids using a normal bioprinting process under the same fabrication conditions as the E-MS-printing without E-field stimulation.

4.5. Hepatogenesis, osteogenesis, and chondrogenesis of hASCs

After culturing hASC-loaded cell constructs in DMEM-L for five days, hepatogenic medium (HM), osteogenic medium (OM), and chondrogenic medium (CDM) were used separately to induce osteogenesis and chondrogenesis of the stem cells, respectively. The HM, OM, and CDM were prepared as follows: HM: 1 × insulin-transferrin-selenium supplement (ITS; Gibco, USA), 10 ng/mL Oncostatin M, 20 ng/mL hepatocyte growth factor (HGF), 10 ng/mL basic fibroblast growth factor (bFGF), 0.1 μM dexamethasone, 5 μM nicotinamide, and 0.1% DMSO were added to the DMEM-L [90,91]; OM: 0.1 μM dexamethasone, 50 μM ascorbic acid, and 10 mM β-glycerol phosphate were added to the DMEM-L [88]; and CDM: 0.1 μM dexamethasone, 50 μM ascorbic acid, transforming growth factor beta 1 (TGF-β1; 10 ng/mL), and 1% ITS+ were added to the DMEM-L [89]. Before using HM, bioprinted hASC-laden structures were washed with HBSS twice and cultured using the DMEM-L containing 0.1% gentamicin (Gibco, USA), 2% FBS, 20 ng/mL endothelial growth factor (EGF), and 10 ng/mL bFGF were added to them for two days [90,91]. All supplements were purchased from Sigma-Aldrich (USA), and OM and CDM were changed every two days.

4.6. In vitro chip-based perfusion system for the 3D liver model

To cultivate the bioprinted *in vitro* hepatic model under a medium perfusion environment, a simple agarose mold-based chip was prepared. Briefly, a negative mold was printed using a Fused Filament Fabrication 3D printer (Cubicon Single Plus; Cubicon Inc., South Korea) and acrylonitrilebutadiene-styrene (ABS)_A100 filament (Cubicon Inc., South Korea), followed by casting an agarose solution (2 wt% in DPBS; Invitrogen, USA) onto the negative mold. CAD software (Shapr3D; Sharp3D.Zrt, Hungary) and the manufacturer's official software (Cubicreator4 V4.2.4, Cubicon Inc., South Korea) were used to design and extract the negative mold into a standard tessellation language file and to create a digital template. The final agarose-based chip, detached from the negative mold, included a compartment for the bioprinted liver

model and attached with autoclaved Teflon tubes (inner diameter: 100 μm). After 7 days of static culture of the 3D liver structures, the *in vitro* liver models were cultured through perfusion of growth medium (20 μL/min [82,83]) using a syringe pump (Fusion 100; Chemyx, USA).

4.7. Characterization of the bioinks and cell constructs

The native tissues, LdECM, LdECM-MA, and printed structures were visualized using a digital single-lens reflex camera (Canon, Japan)-assisted optical microscope (BX FM-32; Olympus, Japan).

To observe the rheological properties, including storage modulus (G') and complex viscosity (η^*), of the prepared bioinks, a rotational rheometer (Bohlin Gemini HR Nano; Malvern Instruments, UK) supplemented with an acrylic parallel-plate geometry (diameter: 40 mm and gap: 200 μm) was used in frequency and time sweep. To observe the effects of E-field, the rheometer was supplemented with a parallel-plate geometry (diameter: 20 mm and gap: 200 μm) equipped with the HVDC power supply. A frequency sweep was conducted with controlled strain (1%) and temperature (25 °C) under 0.1–10 Hz frequency for the bioinks containing various concentrations of ColMA (1.5, 2.5, and 3.5 wt%) and LdECM-MA (2, 3, and 5 wt%). In the case of conducting a time sweep (strain: 1%, temperature: 25 °C, and frequency: 1 Hz), the bioinks were crosslinked with various intensities of exposed UV (0–500 mW/cm^2) for 30 s. Also, the frequency and time sweep were conducted for the ColMA (2.5 wt%) and LldECM-MA (3 wt%) bioinks with and without E-field (1.5 kV/mm). All values are exhibited as means ± standard deviation (SD) (n = 3).

The mechanical properties of the bioprinted structures (6 × 6 × 3 mm^3) under diverse UV conditions (0–600 mW/cm^2) were measured using a SurTA universal testing machine (Chemilab, South Korea) under the compressive mode (compressive rate: 0.1 mm/s) in the wet state. After plotting the stress-strain curves, the compressive moduli were estimated using the linear regions. All values are exhibited as means ± SD (n = 4).

Structural stability of the bioprinted 3D liver model (Experimental structure) was assessed by evaluation of biodegradation rate using growth medium and collagenase (0.1 U/mL in medium). The initial weight (M_i) of the lyophilized structures (3 × 8 × 12 mm^3) was measured, followed by incubation of the samples in the growth medium and collagenase solution for 3, 5, 7, 14, and 21 days. At each time point, the weight of cultured constructs was measured after rinsing with DW and freeze-drying. Optical images of structures in their initial state and after 21 days were captured. The mass loss was calculated by the following equation: Mass loss (%) = $[(M_i - M_d)/M_i] \times 100$. All values are exhibited as means ± SD.

4.8. In vitro cellular activities

Bioprinted cells were stained with live/dead staining solution consisting of 0.15 mM calcein AM (Invitrogen, USA) and 2 mM ethidium homodimer-1 (Invitrogen, USA) dissolved in DMEM for 1 h at 37 °C under 5% CO$_2$ environment to assess the cell viability and the diameter of minispheroids. Following observation of the stained cells with an LSM 700 confocal microscope (Carl Zeiss, Germany) to visualize the live (green) and dead (red) cells, an ImageJ software (National Institutes of Health, USA) was used to estimate the cell viability (n = 4), calculated by observing the number of green and red colored cells, the core diameter and shell thickness of the central vein structure (n = 10), and diameter (n = 100), sphericity (n = 50), and roundness (n = 50) of the formed minispheroids. The sphericity (S_p) and roundness (R_o) were measured using the following equations according to previous studies [66]: $S_p = [d_S^2/(d_L \cdot d_I)]^{1/3}$ (d_S, d_L, and d_I are the diameters of the shortest, longest, and intermediate circles, respectively), and $R_o = (r_1 + r_2 + \cdots + r_n)/n \cdot r_{max}$ (n, r, and r_{max} are the number of corners, radius of the corner curvature, and radius of the maximum inscribed circle, respectively). All values are exhibited as means ± SD.

To observe the formation of minispheroids, 4′,6-diamidino-2-phenylindole (DAPI) (1:100 in DPBS; Invitrogen, USA) and fluorescein phalloidin (1:100 in DPBS; Invitrogen, USA) solution was used to stain the nuclei and actin filament (F-actin) of the printed cells after preparing specimens by fixing (for 1 h at 37 °C) and permeabilizing (for 10 min at 37 °C) the samples using 10% neutral buffered formalin (NBF; Sigma-Aldrich, USA) and 2% Triton X-100. Images of stained nuclei (blue) and F-actin (green) of hASCs were captured using a confocal microscope. The number of sprouts developed in the minispheroids was quantified using ImageJ software. All values are expressed as means ± SD (n = 50).

Cell proliferation of the bioprinted structures was evaluated by performing the MTT assay using the Cell Proliferation Kit I (Boehringer, Germany). Cultured samples were incubated with 3-(4,5-dimethylthiazol-2-yl)-2,5-diphenyltetrazolium bromide (MTT) solution for 4 h, and purple formazan crystals were produced from metabolically active cells. Then, a solubilization solution containing SDS was added to the cells to dissolve the insoluble crystals. An Epoch microplate reader (BioTek) was used to measure the optical density (OD) of the colored solutions at 570 nm. All values are expressed as means ± SD (n = 4).

After culturing the bioprinted structures, the production of albumin and urea was evaluated using Bromocresol Green Albumin and Urea assay kits (Sigma-Aldrich), respectively, according to the manufacturer's protocols. Briefly, following cultivation of the samples in serum-free MEM for 3 days, the supernatant of MEM (5 μL per well) was added to the prepared reagent (200 μL per well) for 5 min, and the expressed albumin levels were detected using a spectrophotometer (absorbance of 620 nm). For urea production, the cultured samples were incubated in Urea Assay buffer (4 °C), followed by incubation of the solution (50 μL) with prepared Reaction Mix (50 μL) at 37 °C for 1 h. The absorbance was measured by the spectrophotometer (absorbance of 570 nm). The amounts of albumin and urea produced were calculated using standard curves from known standards. All values are expressed as means ± SD (n = 3).

Alizarin red S (ARS) staining was performed on the cell constructs to evaluate the calcium content to assess the osteogenesis of the bioprinted hASCs. After fixing the samples using 70% ethanol (Sigma-Aldrich, USA) for 1 h at 4 °C, those were treated with the prepared 40 mM ARS solution (pH 4.2; Sigma-Aldrich, USA) for 1 h at room temperature and rinsed thrice with DW. The optical microscope was used to visualize the stained cell structures, followed by destaining the samples by treatment of 10% cetylpyridinium chloride (Sigma-Aldrich, USA) dissolved in 10 mM sodium phosphate buffer (pH 7.0) for 30 min at room temperature to observe the calcium production. The optical density was measured using a microplate reader (absorbance: 562 nm), and the calcium deposition levels were calculated based on known standards and normalized to the total protein content, which was assessed using the Pierce™ BCA protein assay kit (Thermo Fisher Scientific, USA) according to a previously reported protocol [88]. All values are exhibited as mean ± SDs (n = 4).

To evaluate the chondrogenesis of the printed hASCs, Alcian blue staining was performed on the cultured cell constructs. Following fixation of the hASC-loaded structures cultured with CDM with 10% NBF for 30 min, the samples were incubated in 0.05 wt/v% Alcian blue 8GX (Sigma-Aldrich, USA), which was dissolved in 50 mM sodium acetate buffer (pH 5.8; Sigma-Aldrich, USA) supplemented with 50 mM MgCl$_2$ (Sigma-Aldrich, USA), for 3 h at room temperature. After rinsing the stained samples thrice with 3DW, the blue-colored samples were visualized using an optical microscope. In addition, the GAG content was observed using a Blycan sulfate glycosaminoglycan assay kit. All values are exhibited as mean ± SDs (n = 4).

4.9. Migration and tube formation assay

HepG2 cells and HUVECs were stained with CellTracker™ Green CMFDA (Molecular Probes) to observe cell migration and tube formation. Staining was performed according to the manufacturer's protocol [92]. Briefly, after treatment of prewarmed working solution for the

pre-cultured cells at 37 °C under a 5% CO_2 environment for 30 min, the cells were used to assess the migration and tube formation. Cells were visualized by confocal microscopy.

To assess the effects of hASC minispheroids on HUVEC migration and tube formation and the tube formation ability of HepG2/HUVEC minispheroids, we performed migration and tube formation assays according to previously reported studies [93,94]. HUVECs were seeded onto six-well culture plates at a density of 1.5×10^5 cells/well to conduct the migration assay. After scratching the monolayers with a sterile yellow pipette tip (200 μL) and culturing the cells at 100% confluence, the HUVECs were cultured using conditioned media of bioprinted structures (after 3 days of culture) at 37 °C in a 5% CO_2 environment. The migration area was estimated using ImageJ software. All values are expressed as means ± SD (n = 4).

In the case of tube formation assay, HUVECs or HepG2/HUVEC mixtures were seeded onto the six-well culture plates coated with Matrigel® (Corning, USA). Conditioned media and MEM were used for HUVECs and their mixtures, respectively. Tube formation was observed after 1 day of culture at 37 °C in a 5% CO_2 environment using the confocal microscope. The number of closed loops, junctions, and tube lengths was quantified using an IN Cell Analyzer 2200 (GE Healthcare Life Sciences, UK) and ImageJ software [95]. All values are expressed as means ± SD (n = 4).

4.10. Immunofluorescence analysis

The cultured cell constructs were fixed (for 1 h at 37 °C), blocked (for 2 h at 37 °C), and permeabilized (for 1 h at 37 °C) using 10% NBF, 2% bovine serum albumin (BSA; Sigma-Aldrich, USA), and 2% Triton X-100, respectively to observe the maturation of HepG-2 cells and the differentiation of hASCs and HUVECs. The prepared specimens were treated overnight with mouse anti-albumin (ALB) (5 μg/mL in DPBS; Invitrogen, USA), rabbit anti-E-cadherin (E-cad) (5 μg/mL in DPBS; Invitrogen, USA), rabbit anti-osteopontin (OPN) (5 μg/mL in DPBS; Invitrogen, USA), mouse anti-aggrecan (ACAN) (5 μg/mL in DPBS; Abcam, USA), and rabbit anti-CD31 (5 μg/mL in DPBS; Invitrogen, USA) primary antibodies at 4 °C. The samples were then stained with Alexa Fluor 488-, 594-, and 647-conjugated secondary antibodies (1:50 in DPBS; Invitrogen, USA) for 1 h at 37 °C, based on the host species of the primary antibodies. The nuclei of the cells were counterstained using DAPI (5 μM in DPBS). After visualization of the stained cells with a Carl Zeiss confocal microscope, ALB+, OPN+, ACAN+, and CD31$^+$ areas were quantified using ImageJ software. All values are expressed as means ± SD (n = 3 or 4).

4.11. Gene expression analysis via quantitative reverse transcription polymerase chain reaction (qRT-PCR)

The present study used qRT-PCR to analyze the gene expression based on the $2^{-\Delta\Delta CT}$ method [96]. After isolating the total RNA from the cell constructs by treating TRIzol reagent (Sigma-Aldrich, USA), cDNA was synthesized by performing reverse transcription on the RNase-free DNase-treated RNA using the ReverTraAce™ qPCR RT Master Mix (Toyobo Co., Ltd., Japan). The prepared cDNA and Thunderbird® SYBER® qPCR mix (Toyobo Co., Ltd., Japan) and a StepOnePlus PCR system (Applied Biosystems, USA) were used to conduct the qRT-PCR analysis by assessing threshold cycle (CT) values. The CT values were normalized to the average CT of the reference genes, glyceraldehyde 3-phosphate dehydrogenase (GAPDH) and beta-actin (ACTB), in each sample to calculate the ΔCT. Gene expression results were presented by estimating the comparative fold-change, defined as the geometric mean with error propagation. Statistical analysis was conducted using the ΔCT values [96–98]. The applied primers used are listed in Table S1. All values are reported as mean ± SD (n = 3 or 4).

4.12. Statistical analysis

In this study, a single-factor analysis of variance (ANOVA) (3 or more groups) assisted by Tukey's honest significant difference (HSD) post-hoc test and Student's t-test (two groups) were used to perform statistical analyses via SPSS software (SPSS, Inc., USA). Values of *$p < 0.05$, **$p < 0.01$, and ***$p < 0.001$ were considered significant.

Ethics approval and consent to participate

Not applicable; no animal study; no human subjects.

Data availability statement

The data in this work are available in the manuscript or Supplementary Material, or available from the corresponding author upon reasonable request.

CRediT authorship contribution statement

WonJin Kim: Writing – original draft, Methodology, Investigation, Conceptualization. **GeunHyung Kim:** Writing – review & editing, Supervision, Methodology, Conceptualization.

Declaration of competing interest

The authors (WonJin Kim, GeunHyung Kim) declare that they have no known competing financial interests or personal relationships that could have appeared to influence the work reported in this paper.
none.

Appendix A. Supplementary data

Supplementary data to this article can be found online at https://doi.org/10.1016/j.bioactmat.2024.02.001.

References

[1] S.V. Murphy, A. Atala, 3D bioprinting of tissues and organs, Nat. Biotechnol. 32 (8) (2014) 773–785.

[2] P. Jain, H. Kathuria, N. Dubey, Advances in 3D bioprinting of tissues/organs for regenerative medicine and in-vitro models, Biomaterials 287 (2022) 121639.

[3] C. Yu, W. Zhu, B. Sun, D. Mei, M. Gou, S. Chen, Modulating physical, chemical, and biological properties in 3D printing for tissue engineering applications, Appl. Phys. Rev. 5 (4) (2018) 041107.

[4] W. Kim, G. Kim, Bioprinting 3D muscle tissue supplemented with endothelial-spheroids for neuromuscular junction model, Appl. Phys. Rev. 10 (3) (2023) 031410.

[5] J. Kim, G. Kim, Formation of various cell-aggregated structures in the core of hydrogel filament using a microfluidic device and its application as an in vitro neuromuscular junction model, Chem. Eng. J. 472 (2023) 144979.

[6] J. Lee, H. Lee, E.-J. Jin, D. Ryu, G.H. Kim, 3D bioprinting using a new photo-crosslinking method for muscle tissue restoration, NPJ Regen. Med. 8 (1) (2023) 18.

[7] H. Hwangbo, H. Lee, E.-J. Jin, J. Lee, Y. Jo, D. Ryu, G. Kim, Bio-printing of aligned GelMa-based cell-laden structure for muscle tissue regeneration, Bioact, Mater 8 (2022) 57–70.

[8] T. Zandrini, S. Florczak, R. Levato, A. Ovsianikov, Breaking the resolution limits of 3D bioprinting: future opportunities and present challenges, Trends Biotechnol. 41 (5) (2022) 604–614.

[9] S. Rahmani Dabbagh, M. Rezapour Sarabi, M.T. Birtek, N. Mustafaoglu, Y.S. Zhang, S. Tasoglu, 3D bioprinted organ-on-chips, Aggregate 4 (1) (2023) e197.

[10] M.V. Monteiro, Y.S. Zhang, V.M. Gaspar, J.F. Mano, 3D-bioprinted cancer-on-a-chip: level-up organotypic in vitro models, Trends Biotechnol. 40 (4) (2022) 432–447.

[11] A. Mazzocchi, S. Soker, A. Skardal, 3D bioprinting for high-throughput screening: drug screening, disease modeling, and precision medicine applications, Appl. Phys. Rev. 6 (1) (2019) 011302.

[12] B. Jin, Y. Liu, S. Du, X. Sang, H. Yang, Y. Mao, Current trends and research topics regarding liver 3D bioprinting: a bibliometric analysis research, Front. Cell Dev. Biol. 10 (2022) 1047524.

[13] L. Ma, Y. Wu, Y. Li, A. Aazmi, H. Zhou, B. Zhang, H. Yang, Current advances on 3D-bioprinted liver tissue models, Adv. Healthcare Mater. 9 (24) (2020) 2001517.

[14] C. Zhong, H.-Y. Xie, L. Zhou, X. Xu, S.-S. Zheng, Human hepatocytes loaded in 3D bioprinting generate mini-liver, Hepatobiliary Pancreat. Dis. Int. 15 (5) (2016) 512–518.

[15] M. Cuvellier, F. Ezan, H. Oliveira, S. Rose, J.-C. Fricain, S. Langouët, V. Legagneux, G. Baffet, 3D culture of HepaRG cells in GelMa and its application to bioprinting of a multicellular hepatic model, Biomaterials 269 (2021) 120611.

[16] J. He, J. Wang, Y. Pang, H. Yu, X. Qin, K. Su, T. Xu, H. Ren, Bioprinting of a hepatic tissue model using human-induced pluripotent stem cell-derived hepatocytes for drug-induced hepatotoxicity evaluation, Int. J. Bioprinting 8 (3) (2022) 581.

[17] R. Taymour, N.A. Chicaiza-Cabezas, M. Gelinsky, A. Lode, Core–shell bioprinting of vascularized in vitro liver sinusoid models, Biofabrication 14 (4) (2022) 045019.

[18] Y. Yang, Z. Yu, X. Lu, J. Dai, C. Zhou, J. Yan, L. Wang, Z. Wang, J. Zang, Minimally invasive bioprinting for in situ liver regeneration, Bioact. Mater. 26 (2023) 465–477.

[19] X. Ma, X. Qu, W. Zhu, Y.-S. Li, S. Yuan, H. Zhang, J. Liu, P. Wang, C.S.E. Lai, F. Zanella, Deterministically patterned biomimetic human iPSC-derived hepatic model via rapid 3D bioprinting, Proc. Natl. Acad. Sci. USA 113 (8) (2016) 2206–2211.

[20] Q. Mao, Y. Wang, Y. Li, S. Juengpanich, W. Li, M. Chen, J. Yin, J. Fu, X. Cai, Fabrication of liver microtissue with liver decellularized extracellular matrix (dECM) bioink by digital light processing (DLP) bioprinting, Mater. Sci. Eng. C 109 (2020) 110625.

[21] D. Kang, G. Hong, S. An, I. Jang, W.S. Yun, J.H. Shim, S. Jin, Bioprinting of multiscaled hepatic lobules within a highly vascularized construct, Small 16 (13) (2020) 1905505.

[22] S.V. Murphy, P. De Coppi, A. Atala, Opportunities and challenges of translational 3D bioprinting, Nat. Biomed. Eng. 4 (4) (2020) 370–380.

[23] S. Vijayavenkataraman, W.-C. Yan, W.F. Lu, C.-H. Wang, J.Y.H. Fuh, 3D bioprinting of tissues and organs for regenerative medicine, Adv. Drug Deliv. Rev. 132 (2018) 296–332.

[24] N. Ashammakhi, S. Ahadian, C. Xu, H. Montazerian, H. Ko, R. Nasiri, N. Barros, A. Khademhosseini, Bioinks and bioprinting technologies to make heterogeneous and biomimetic tissue constructs, Mater. Today Bio 1 (2019) 100008.

[25] A. GhavamiNejad, N. Ashammakhi, X.Y. Wu, A. Khademhosseini, Crosslinking strategies for 3D bioprinting of polymeric hydrogels, Small 16 (35) (2020) 2002931.

[26] R. Levato, T. Jungst, R.G. Scheuring, T. Blunk, J. Groll, J. Malda, From shape to function: the next step in bioprinting, Adv. Mater. 32 (12) (2020) 1906423.

[27] J. Hauptstein, L. Forster, A. Nadernezhad, H. Horder, P. Stahlhut, J. Groll, T. Blunk, J. Teßmar, Bioink platform utilizing dual-stage crosslinking of hyaluronic acid tailored for chondrogenic differentiation of mesenchymal stromal cells, Macromol. Biosci. 22 (2) (2022) 2100331.

[28] G.L. Ying, N. Jiang, S. Maharjan, Y.X. Yin, R.R. Chai, X. Cao, J.Z. Yang, A.K. Miri, S. Hassan, Y.S. Zhang, Aqueous two-phase emulsion bioink-enabled 3D bioprinting of porous hydrogels, Adv. Mater. 30 (50) (2018) 1805460.

[29] J.P. Armstrong, M. Burke, B.M. Carter, S.A. Davis, A.W. Perriman, 3D bioprinting using a templated porous bioink, Adv. Healthcare Mater. 5 (14) (2016) 1724–1730.

[30] H. Hwangbo, H. Lee, E.J. Jin, Y. Jo, J. Son, H.M. Woo, D. Ryu, G.H. Kim, Photosynthetic cyanobacteria can clearly induce efficient muscle tissue regeneration of bioprinted cell-constructs, Adv. Funct. Mater. 33 (10) (2023) 2209157.

[31] N.G. Willemen, S. Hassan, M. Gurian, M.F. Jasso-Salazar, K. Fan, H. Wang, M. Becker, I.E. Allijn, A. Bal-Öztürk, J. Leijten, Enzyme-mediated alleviation of peroxide toxicity in self-oxygenating biomaterials, Adv. Healthcare Mater. 11 (13) (2022) 2102697.

[32] N. Majumder, A. Mishra, S. Ghosh, Effect of varying cell densities on the rheological properties of the bioink, Bioprinting 28 (2022) e00241.

[33] W. Kim, H. Lee, C.K. Lee, J.W. Kyung, S.B. An, I.B. Han, G.H. Kim, A bioprinting process supplemented with in situ electrical stimulation directly induces significant myotube formation and myogenesis, Adv. Funct. Mater. 31 (51) (2021) 2105170.

[34] B. Lu, M. Ye, J. Xia, Z. Zhang, Z. Xiong, T. Zhang, Electrical stimulation promotes the vascularization and functionalization of an engineered biomimetic human cardiac tissue, Adv. Healthcare Mater. (2023) 2300607.

[35] J.Y. Ma, Y.X. Wang, Y. Huang, Y. Zhang, Y.X. Cui, D.M. Kong, Chemical–biological approaches for the direct regulation of cell–cell aggregation, Aggregate 3 (2) (2022) e166.

[36] M. Ravi, V. Paramesh, S. Kaviya, E. Anuradha, F.P. Solomon, 3D cell culture systems: advantages and applications, J. Cell. Physiol. 230 (1) (2015) 16–26.

[37] E. Fennema, N. Rivron, J. Rouwkema, C. van Blitterswijk, J. De Boer, Spheroid culture as a tool for creating 3D complex tissues, Trends Biotechnol. 31 (2) (2013) 108–115.

[38] J. Yamamoto, M. Udono, S. Miura, S. Sekiya, A. Suzuki, Cell aggregation culture induces functional differentiation of induced hepatocyte-like cells through activation of Hippo signaling, Cell Rep. 25 (1) (2018) 183–198.

[39] C. Yuasa, Y. Tomita, M. Shono, K. Ishimura, A. Ichihara, Importance of cell aggregation for expression of liver functions and regeneration demonstrated with primary cultured hepatocytes, J. Cell. Physiol. 156 (3) (1993) 522–530.

[40] D.F. Duarte Campos, C.D. Lindsay, J.G. Roth, B.L. LeSavage, A.J. Seymour, B.A. Krajina, R. Ribeiro, P.F. Costa, A. Blaeser, S.C. Heilshorn, Bioprinting cell-and spheroid-laden protein-engineered hydrogels as tissue-on-chip platforms, Front. Bioeng. Biotechnol. 8 (2020) 374.

[41] B.A. de Melo, Y.A. Jodat, S. Mehrotra, M.A. Calabrese, T. Kamperman, B.B. Mandal, M.H. Santana, E. Alsberg, J. Leijten, S.R. Shin, 3D printed cartilage-like tissue constructs with spatially controlled mechanical properties, Adv. Funct. Mater. 29 (51) (2019) 1906330.

[42] N. Mekhileri, K. Lim, G. Brown, I. Mutreja, B. Schon, G. Hooper, T. Woodfield, Automated 3D bioassembly of micro-tissues for biofabrication of hybrid tissue engineered constructs, Biofabrication 10 (2) (2018) 024103.

[43] T. Imamura, M. Shimamura, T. Ogawa, T. Minagawa, T. Nagai, S. Silwal Gautam, O. Ishizuka, Biofabricated structures reconstruct functional urinary bladders in radiation-injured rat bladders, Tissue Eng. 24 (21–22) (2018) 1574–1587.

[44] B. Ayan, D.N. Heo, Z. Zhang, M. Dey, A. Povilianskas, C. Drapaca, I.T. Ozbolat, Aspiration-assisted bioprinting for precise positioning of biologics, Sci. Adv. 6 (10) (2020) eaaw5111.

[45] S. Jeon, J.H. Heo, M.K. Kim, W. Jeong, H.W. Kang, High-precision 3D bio-dot printing to improve paracrine interaction between multiple types of cell spheroids, Adv. Funct. Mater. 30 (2020) 2005324.

[46] A.C. Daly, D.J. Kelly, Biofabrication of spatially organised tissues by directing the growth of cellular spheroids within 3D printed polymeric microchambers, Biomaterials 197 (2019) 194–206.

[47] W. Kim, G. Kim, Hybrid cell constructs consisting of bioprinted cell-spheroids, Bioeng. Transl. Med. (2022) e10397.

[48] T. Anada, J. Fukuda, Y. Sai, O. Suzuki, An oxygen-permeable spheroid culture system for the prevention of central hypoxia and necrosis of spheroids, Biomaterials 33 (33) (2012) 8430–8441.

[49] G. Hamilton, Multicellular spheroids as an in vitro tumor model, Cancer Lett. 131 (1) (1998) 29–34.

[50] M. Koblenzer, M. Weiler, A. Fragoulis, T. Rütten, T. Pufe, H. Jahr, Physiological mineralization during in vitro osteogenesis in a biomimetic spheroid culture model, Cells 11 (17) (2022) 2702.

[51] K. Zhang, S. Yan, G. Li, L. Cui, J. Yin, In-situ birth of MSCs multicellular spheroids in poly (L-glutamic acid)/chitosan scaffold for hyaline-like cartilage regeneration, Biomaterials 71 (2015) 24–34.

[52] X. Zhu, Q. Wu, Y. He, M. Gao, Y. Li, W. Peng, S. Li, Y. Liu, R. Zhang, J. Bao, Fabrication of size-controllable and arrangement-orderly HepG2 spheroids for drug screening via decellularized liver matrix-derived micropattern array chips, ACS Omega 7 (2) (2022) 2364–2376.

[53] G.R. Pesch, F. Du, A review of dielectrophoretic separation and classification of non-biological particles, Electrophoresis 42 (1–2) (2021) 134–152.

[54] G. Kim, Y.M. Shkel, Polymeric composites tailored by electric field, J. Mater. Res. 19 (4) (2004) 1164–1174.

[55] J. Happel, H. Brenner, Low Reynolds Number Hydrodynamics: with Special Applications to Particulate Media, Springer Science & Business Media, 1983.

[56] L.D. Landau, J.S. Bell, M. Kearsley, L. Pitaevskii, E. Lifshitz, J. Sykes, Electrodynamics of Continuous Media, elsevier, 2013.

[57] R. Pethig, Dielectrophoresis: status of the theory, technology, and applications, Biomicrofluidics 4 (2) (2010) 022811.

[58] A. Sebastian, A.G. Venkatesh, G.H. Markx, Tissue engineering with electric fields: Investigation of the shape of mammaliancell aggregates formed at interdigitateddoppositely castellated electrodes, Electrophoresis 28 (2007) 3821–3828.

[59] K. Mogi, C. Shirataki, K. Kihara, H. Kuwahara, Y. Hongoh, T. Yamamoto, Trapping and isolation of single prokaryotic cells in a micro-chamber array using dielectrophoresis, RSC Adv. 6 (2016) 113000–113006.

[60] J. Cottet, A. Kehren, S. Lasli, H. van Lintel, F. Buret, M. Frénéa-Robin, P. Renaud, Dielectrophoresis-assisted creation of cell aggregates under flow conditions using planar electrodes, Electrophoresis 40 (10) (2019) 1498–1509.

[61] D.R. Albrecht, G.H. Underhill, T.B. Wassermann, R.L. Sah, S.N. Bhatia, Probing the role of multicellular organization in three-dimensional microenvironments, Nat. Methods 3 (2006) 369–375.

[62] M. Punjiya, H.R. Nejad, J. Mathews, M. Levin, S. Sonkusale, A flow through device for simultaneous dielectrophoretic cell trapping and AC electroporation, Sci. Rep. 9 (2019) 11988.

[63] G.H. Yang, W. Kim, J. Kim, G. Kim, A skeleton muscle model using GelMA-based cell-aligned bioink processed with an electric-field assisted 3D/4D bioprinting, Theranostics 11 (1) (2021) 48.

[64] L. Ouyang, R. Yao, Y. Zhao, W. Sun, Effect of bioink properties on printability and cell viability for 3D bioplotting of embryonic stem cells, Biofabrication 8 (3) (2016) 035020.

[65] E. Gevaert, L. Dolle, T. Billiet, P. Dubruel, L. van Grunsven, A. van Apeldoorn, R. Cornelissen, High throughput micro-well generation of hepatocyte micro-aggregates for tissue engineering, PLoS One 9 (8) (2014) e105171.

[66] I. Cruz-Matías, D. Ayala, D. Hiller, S. Gutsch, M. Zacharias, S. Estradé, F. Peiró, Sphericity and roundness computation for particles using the extreme vertices model, J. Comput. Sci. 30 (2019) 28–40.

[67] I. Song, B.S. Kim, C.S. Kim, G.I. Im, Effects of BMP-2 and vitamin D3 on the osteogenic differentiation of adipose stem cells, Biochem. Biophys. Res. Commun. 408 (2011) 126–131.

[68] A.T. Mehlhorn, P. Niemeyer, S. Kaiser, G. Finkenzeller, G.B. Stark, N.P. Südkamp, H. Schmal, Differential expression pattern of extracellular matrix molecules during

chondrogenesis of mesenchymal stem cells from bone marrow and adipose tissue, Tissue Eng. 12 (2016) 2853–2862.

[69] M. Štampar, J. Tomc, M. Filipič, B. Žegura, Development of in vitro 3D cell model from hepatocellular carcinoma (HepG2) cell line and its application for genotoxicity testing, Arch. Toxicol. 93 (2019) 3321–3333.

[70] P. Carabias, M.V. Espelt, M.L. Bacigalupo, P. Rojas, L. Sarrias, A. Rubin, N. A. Saffioti, M.T. Elola, J.P. Rossi, C. Wolfenstein-Todel, G.A. Rabinovich, M. F. Troncoso, Galectin-1 confers resistance to doxorubicin in hepatocellular carcinoma cells through modulation of P-glycoprotein expression, Cell Death Dis. 13 (2022) 79.

[71] M.R. Love, S. Palee, S.C. Chattipakorn, N. Chattipakorn, Effects of electrical stimulation on cell proliferation and apoptosis, J. Cell. Physiol. 233 (3) (2018) 1860–1876.

[72] G. Xu, Z. Ding, Q. Lu, X. Zhang, X. Zhou, L. Xiao, G. Lu, D.L. Kaplan, Electric field-driven building blocks for introducing multiple gradients to hydrogels, Protein Cell 11 (4) (2020), 267-241.

[73] D. Kittipoomwong, D.J. Klingenberg, Y.M. Shkel, J.F. Morris, J.C. Ulicny, Transient behavior of electrorheological fluids in shear flow, J. Rheol. 52 (1) (2008) 225.

[74] C.R. Thoma, M. Zimmermann, I. Agarkova, J.M. Kelm, W. Krek, 3D cell culture systems modeling tumor growth determinants in cancer target discovery, Adv. Drug Deliv. Rev. 69 (2014) 29–41.

[75] M. Mustafa, G.E.-D.A. Abuo-Rahma, A.A. Abd El-Hafeez, E.R. Ahmed, D. Abdelhamid, P. Ghosh, A.M. Hayallah, Discovery of antiproliferative and anti-FAK inhibitory activity of 1, 2, 4-triazole derivatives containing acetamido carboxylic acid skeleton, Bioorg. Med. Chem. Lett 40 (2021) 127965.

[76] D. Gnani, I. Romito, S. Artuso, M. Chierici, C. De Stefanis, N. Panera, A. Crudele, S. Ceccarelli, E. Carcarino, V. D'Oria, Focal adhesion kinase depletion reduces human hepatocellular carcinoma growth by repressing enhancer of zeste homolog 2, Cell Death Differ. 24 (5) (2017) 889–902.

[77] K.H. Hussein, K.M. Park, J.H. Ghim, S.R. Yang, H.M. Woo, Three dimensional culture of HepG2 liver cells on a rat decellularized liver matrix for pharmacological studies, J. Biomed. Mater. Res. Part B Appl. Biomater. 104 (2) (2016) 263–273.

[78] H. Lee, S. Chae, J.Y. Kim, W. Han, J. Kim, Y. Choi, D.W. Cho, Cell-printed 3D liver-on-a-chip possessing a liver microenvironment and biliary system, Biofabrication 11 (2) (2019) 025001.

[79] H.J. Cho, H.J. Kim, K.J. Lee, S. Lasli, A. Ung, T. Hoffman, R. Nasiri, P. Bandaru, S. Ahadian, M.R. Dokmeci, J. Lee, A. Khademhosseini, Bioengineered multicellular liver microtissues for modeling advanced hepatic fibrosis driven through non-alcoholic fatty liver disease, Small 17 (14) (2021) 2007425.

[80] J.B. Lee, J.S. Park, Y.M. Shin, D.H. Lee, J.K. Yoon, D.H. Kim, U.H. Ko, Y.T. Kim, S. H. Bae, H.J. Sung, Implantable vascularized liver chip for cross-validation of disease treatment with animal model, Adv. Funct. Mater. 29 (23) (2019) 1900075.

[81] G.G.Y. Chiew, A. Fu, K. Perng Low, K. Qian Luo, Physical supports from liver cancer cells are essential for differentiation and remodeling of endothelial cells in a HepG2-HUVEC co-culture model, Sci. Rep. 5 (1) (2015) 10801.

[82] X. Liu, X. Wang, L. Zhang, L. Sun, H. Wang, H. Zhao, Z. Zhang, W. Liu, Y. Huang, S. Ji, J. Zhang, K. Li, B. Song, C. Li, H. Zhang, S. Li, S. Wang, X. Zheng, Q. Gu, 3D liver tissue model with branched vascular networks by multimaterial bioprinting, Adv. Healthcare Mater. 10 (2021) 2101405.

[83] G. Gao, W. Park, B.S. Kim, M. Ahn, S. Chae, W.W. Cho, J. Kim, J.Y. Lee, J. Jang, D. W. Cho, Construction of a novel in vitro atherosclerotic model from geometry-tunable artery equivalents engineered via in-bath coaxial cell printing, Adv. Funct. Mater. 31 (10) (2021) 2008878.

[84] L. Ma, Y. Wu, Y. Li, A. Aazmi, H. Zhou, B. Zhang, H. Yang, Current advances on 3D-bioprinted liver tissue models, Adv. Healthcare Mater. 9 (2020) 2001517.

[85] W. Kim, G.H. Kim, Highly bioactive cell-laden hydrogel constructs bioprinted using an emulsion bioink for tissue engineering applications, Biofabrication 14 (4) (2022) 045018.

[86] W. Kim, H. Lee, J. Lee, A. Atala, J.J. Yoo, S.J. Lee, G.H. Kim, Efficient myotube formation in 3D bioprinted tissue construct by biochemical and topographical cues, Biomaterials 230 (2020) 119632, https://doi.org/10.1016/j.biomaterials.2019.119632.

[87] G. Mattei, V. Di Patria, A. Tirella, A. Alaimo, G. Elia, A. Corti, A. Paolicchi, A. Ahluwalia, Mechanostructure and composition of highly reproducible decellularized liver matrices, Acta Biomater. 10 (2) (2014) 875–882.

[88] W. Kim, H. Lee, E.J. Roh, S.B. An, I.-B. Han, G.H. Kim, A multicellular bioprinted cell construct for vascularized bone tissue regeneration, Chem. Eng. J. 431 (2022) 133882.

[89] Y.W. Koo, C.S. Lim, A. Darai, J. Lee, W. Kim, I. Han, G.H. Kim, Shape-memory collagen scaffold combined with hyaluronic acid for repairing intervertebral disc, Biomater. Res. 27 (1) (2023) 1–21.

[90] A. Banas, T. Teratani, Y. Yamamoto, M. Tokuhara, F. Takeshita, G. Quinn, H. Okochi, T. Ochiya, Adipose tissue-derived mesenchymal stem cells as a source of human hepatocytes, Hepatology 46 (1) (2007) 219–228.

[91] H. Lee, Y.B. Kim, S.H. Ahn, J.S. Lee, C.H. Jang, H. Yoon, W. Chun, G.H. Kim, A new approach for fabricating collagen/ECM-based bioinks using preosteoblasts and human adipose stem cells, Adv. Healthcare Mater. 4 (9) (2015) 1359–1368.

[92] W. Kim, G.H. Kim, An intestinal model with a finger-like villus structure fabricated using a bioprinting process and collagen/SIS-based cell-laden bioink, Theranostics 10 (6) (2020) 2495.

[93] R.A. Francescone III, M. Faibish, R. Shao, A Matrigel-based tube formation assay to assess the vasculogenic activity of tumor cells, J. Vis. Exp. 55 (2011) e3040.

[94] C.-C. Liang, A.Y. Park, J.-L. Guan, In vitro scratch assay: a convenient and inexpensive method for analysis of cell migration in vitro, Nat. Protoc. 2 (2) (2007) 329–333.

[95] G. Carpentier, S. Berndt, S. Ferratge, W. Rasband, G. Cuendet, G. Uzan, P. Albanese, Angiogenesis analyzer for ImageJ—a comparative morphometric analysis of "endothelial tube formation assay" and "fibrin bead assay", Sci. Rep. 10 (1) (2020) 11568.

[96] K.J. Livak, T.D. Schmittgen, Analysis of relative gene expression data using real-time quantitative PCR and the 2− ∆∆CT method, Methods 25 (4) (2001) 402–408.

[97] S.A. Bustin, V. Benes, J.A. Garson, J. Hellemans, J. Huggett, M. Kubista, R. Mueller, T. Nolan, M.W. Pfaffl, G.L. Shipley, The MIQE Guidelines: M Inimum I Nformation for Publication of Q Uantitative Real-Time PCR E Xperiments, Oxford University Press, 2009.

[98] J. Vandesompele, K. De Preter, F. Pattyn, B. Poppe, N. Van Roy, A. De Paepe, F. Speleman, Accurate normalization of real-time quantitative RT-PCR data by geometric averaging of multiple internal control genes, Genome Biol. 3 (7) (2002) 1–12.